Title

Drainage in Geological Materials at Intermediate Scales

Author

Breen, Stephen

Publication Date

2020

Peer reviewed|Thesis/dissertation

Drainage in Geological Materials at Intermediate Scales

by

Stephen J. Breen

A dissertation submitted in partial satisfaction of the

requirements for the degree of

Doctor of Philosophy

in

Earth and Planetary Science

in the

Graduate Division

of the

University of California, Berkeley

Committee in charge:

Professor Michael Manga, Chair
Professor Imke de Pater
Professor James Sethian

Fall 2020

Drainage in Geological Materials at Intermediate Scales

Abstract

Drainage in Geological Materials at Intermediate Scales

by

Stephen J. Breen

Doctor of Philosophy in Earth and Planetary Science

University of California, Berkeley

Professor Michael Manga, Chair

The disconnect between pore-scale processes and continuum models of porous flow is a persistent problem in hydrogeology. Here, we present two drainage studies which attempt to bridge this divide. In the first, we demonstrate the sensitivity of continuum-scale drainage simulations to the critical nonwetting saturation, which is the saturation state of a voxel when nonwetting phase permeability becomes nonzero. To give this parameter a physical basis, we use laboratory observations of drainage in thin, backlit bead packs and Invasion Percolation simulations to propose a new percolation model for saturation as a function of distance behind the drainage front, incorporating Bond and capillary number dependency. In the second study, motivated by observations of streamflow responses to earthquakes, we test the hypothesis that seismic shaking can drain water out of the unsaturated zone. To accomplish this, we construct a sand chamber and monitor pore pressure during impact-induced shaking. We identify three distinct mechanisms: consolidation of sediments in the saturated zone, release of capillary water from the capillary fringe, and mobilization of isolated pore water in the unsaturated zone.

To Robert Kennedy (1989 - 2011, B.S. Physics) and Tobias Lochbühler (1984 - 2014, PhD Geophysics), for their friendship, the science we did together, and the discoveries they would have made.

Contents

List of Figures

List of Tables

Acknowledgments

We fill pages with text and images to figure out what we think, to collect our ideas, give them life, and, ultimately, to move on from them. I have been fortunate to learn this skill, and as I look ahead to the next challenge, I am deeply thankful for the teachers at Berkeley who carefully read, criticized, and contributed to my work. While training me to become an independent scientist, they also taught me that the job cannot be done alone. Michael Manga has opened more doors than I could walk through, and his feedback on this manuscript was always fast and incisive. I am, moreover, thankful for his exemplary academic leadership, particularly at this difficult juncture in history. In 2013, I came to Berkeley intending to study porous flow and was glad to connect with Steve Pride over this shared interest. Steve's mathematical insights were immensely helpful for Chapter 1, and I am grateful for the urgency and wonder that he brings to every scientific endeavor. More recently, Chi Wang invited me to collaborate with him and a visiting undergraduate to study the relationship between seismic energy and pore pressure. Our results are described in Chapter 2. I appreciate Chi for his extraordinary attention to detail, from the laboratory to the manuscript, and for being a model of scientific originality and productivity. I am also thankful to Imke de Pater for welcoming me into her research group and sharing her expertise as we conducted electromagnetic forward and inverse modeling studies of the lunar interior. Some of the computational routines I developed with her are running behind the scenes in Chapter 1 and have been shared with other researchers. Thanks also to James Sethian for his enlightening course on numerical methods (Math 228b), for serving on my committees, and for providing helpful suggestions to broaden this manuscript's appeal.

I am also grateful to Robert Citron for being a supportive friend and colleague through the ups and downs of graduate school, to Noah Randolph-Flagg for welcoming me to Berkeley and teaching me so much about geology, to Heidi Fuqua Haviland for helping me navigate the qualifying exam, to Seth Saltiel for being an excellent peer advisor and a connection at LBNL, to Ruby Fu for many motivating conversations about porous flow, to Yder Masson for assistance with iPerc, to Greg Delory for his research guidance in my first and second years, to John Grimsich for building experiments with me, to Dayong Wang for a fruitful collaboration on CO_2 sequestration, to Betsy Mitchell for coaching me through outreach experiences at the Be a Scientist program and the Alameda Elementary Environmental Literacy Summer Institute, to Charles Satchell for strengthening me with many years of martial arts training, to Eti Valdez-Kaminsky for helping me find paths through the blizzards of life and work, and, finally, to the talented undergraduates who I met in the lab, particularly Zifan Zhang and Dakota Churchill, and the small but nimble group who suffered diligently through my first time instructing EPS 50 (Planet Earth). It has been a privilege to learn from all of these brilliant people.

I would like to acknowledge financial support from the Chemical Sciences, Geosciences and Biosciences Division of the DOE Office of Science's Basic Energy Sciences (BES) program, and from the National Science Foundation, Division of Earth Sciences.

Finally, I owe everything to my family and oldest friends: Louise Costigan-Kerns, Ralph Kerns (1946-2009), Jacqueline Kerns, Karen Smith, Christopher Harris, Mark Hendrickson, Tom Costigan, Travis Allyn, Ahmad Sghayer, Joshua Tully, Allen Young, Ryan Sather, Peter Sauer, Giuseppe Astarita, and Joe Labozetta. I would be nowhere without their love, support, and patience.

> *Work diligently. Diligently. Work patiently and persistently. Patiently and persistently. And you are bound to be successful. Bound to be successful.*
>
> -S. N. Goenka

Chapter 1

Overview

During drainage, a nonwetting fluid displaces a wetting fluid in a porous material. A ubiquitous example of this process, and the main focus of this thesis, is air displacing water in rocks, sands, and soils. Behind the air/water drainage front which marks the boundary between single and multiphase flow, the saturation structure is determined by the relative influence of capillary, gravitational, and viscous forces, expressed by the dimensionless Bond number (Bo, the ratio of gravitational to capillary forces), Capillary number (Ca, the ratio of viscous to capillary forces), and viscosity ratio.

Because the details of the pore network are unknown, drainage models assume the existence of a representative elementary volume (REV), which, in principle, is large enough so that the average is well behaved and small enough to avoid averaging over larger trends in variables such as saturation and permeability. The REV defines a linear scale above which a viscous flow law called Darcy's law applies. Once it is established, we build a discretized model of the subsurface and solve a pair of coupled Darcy equations for each phase, with constitutive functions describing the saturation-dependence of capillary pressure and relative permeability. These equations are given at the beginning of Chapter 2.

This "standard model" has frustrated engineers and scientists alike as they try to understand, for instance, transport in the shallow unsaturated zone, the fate of geologically sequestered carbon dioxide, or the formation of ore deposits. Its most important shortcomings are that: (1) real geological materials show correlations across a broad range of length scales, and therefore REVs may not exist; (2) transport of both phases near the drainage front is not laminar, as assumed by Darcy's law, but instead occurs in sharp bursts called Haines jumps when fluid pressure overcomes resistance at the meniscus; (3) the forms of the constitutive permeability and capillary pressure functions are not understood in terms of fundamental pore geometry or fluid property variables, but are instead based on idealized bundle-of-tubes models; and (4) the predictive power of the standard model is weak, and therefore in practice it is deployed as a history matching tool with enough knobs to match any data, and without the expectation that the calibrated subsurface model is accurate or will predict the correct outputs if the inputs change.

These problems present an opportunity to answer some fascinating and important scientific questions, such as: (1) what are the scaling properties of immiscible flows, and how do we formulate transport equations that capture them?; (2) what equations should replace Darcy's law in regions of non-laminar flow?; and (3) can discrete models of porous flow reveal universal features of real flows? In a series of papers, Wilkinson and Willemsen (1983, 1984, and 1986) began addressing these questions by inventing a new form of percolation theory called Invasion Percolation (IP). In contrast to ordinary percolation, which describes static structures that are created by instantaneously populating a lattice, IP is a dynamic model of transport wherein lattice sites (representing pores) are populated sequentially. Surprisingly, Wilkinson and Willemsen found that the structures produced by IP were broadly similar to those of ordinary percolation. The 2D and 3D fractal dimensions were equivalent, for instance, and the occupation fraction at the point of percolation, when the invader first forms a connected path across the lattice, was close to the percolation threshold in sufficiently large systems. In the 90s and 00s, Wilkinson's results motivated a series of drainage experiments in 2D networks which demonstrated, remarkably, that the areal scaling of real flows matches the predictions of percolation theory.

Chapter 2 carries this research forward with new observations of drainage in three-dimensional systems and a systematic exploration of the influence of viscous and gravitational forces on saturation profiles. We observe how saturation curves distort with varying Bo using Invasion Percolation simulations, and with varying Ca using novel laboratory experiments which utilize light transmission to monitor water saturation in bead chambers. Both sets of observations are new to the porous flow literature. We use them to constrain a percolation-based model for saturation as a function of position behind the drainage front. After demonstrating significant disagreements between TOUGH2 "standard model" simulations and the laboratory experiments, we propose our saturation model as a basis for predicting the saturation state of a frontal voxel at percolation, which in the "standard model" is represented by the relative permeability endpoint.

In Chapter 3 we examine the relationship between seismic shaking and drainage. Earthquakes interact with water in a variety of interesting ways. For instance, during earthquakes, streamflow and groundwater level may increase, as occurred following a recent earthquake swarm in Puerto Rico. The mechanisms for such changes, however, are still unclear. In this chapter, we measure the response of pore pressure to seismic shaking to test the hypothesis that earthquakes can cause shallow groundwater to flow toward streams. To accomplish this, we built a tall sand column, filled it with water, and instrumented it with sensors that measure how pore pressure responds when the chamber is shaken by an impact. We found that trapped water in the shallow subsurface, which is held in place by adhesive forces between sand and water, can be released to the water table by seismic shaking, where it can then flow toward a stream.

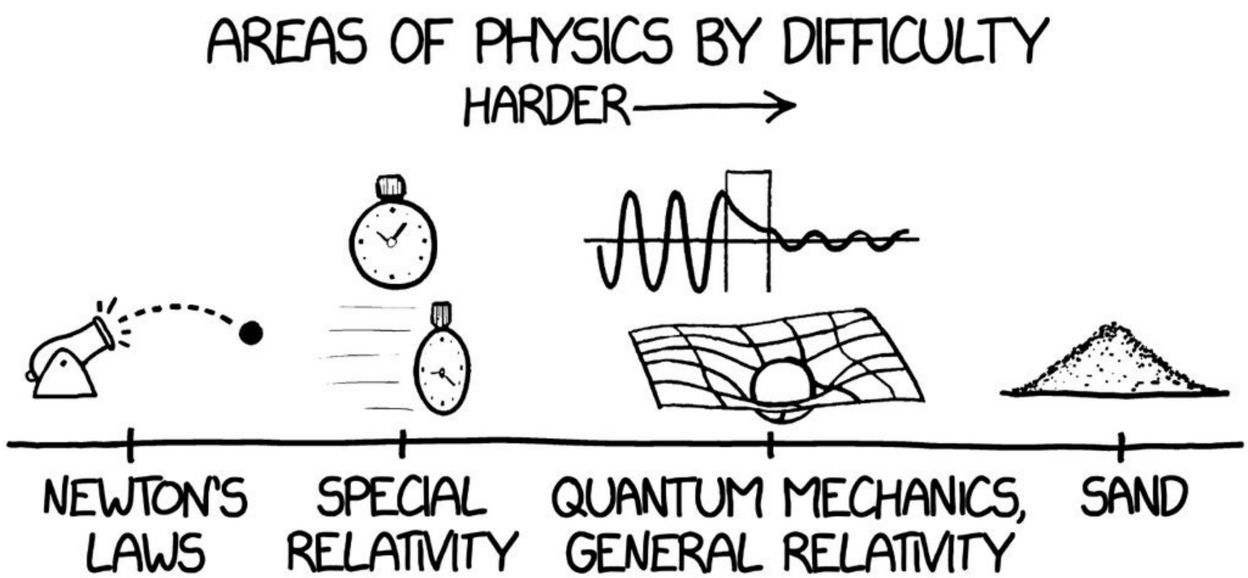

Figure 1.1: Munroe, Randall. “What Makes Sand Soft?” *The New York Times*, 10 Nov. 2020, Section D, p. 4.

Chapter 2

Stable drainage in a gravity field

2.1 Summary

During drainage, as a voxel of porous material is being actively invaded prior to percolation, the invading nonwetting fluid cannot be transmitted to the neighboring downstream voxel until a critical nonwetting saturation S_{nc} is reached. This occurs when the invading fluid forms a percolating path across the voxel. We present novel laboratory observations of gravitationally stable, air/water drainage in thin bead packs, with 2D saturation fields monitored at high spatial and temporal resolution using transmitted light. We also present Invasion Percolation simulations. Both sets of observations show that S_{nc} has a strong dependence on capillary number (Ca), Bond number (Bo), and voxel size (L_z). We propose a percolation model that describes the functional form of $S_{nc}(\mathrm{Bo}, \mathrm{Ca}, L_z)$.

2.2 Introduction

A macroscopic, porous-continuum theory of multiphase, immiscible flow in geological materials must provide equations for the spatial and temporal evolution of the saturations and average fluid pressures of each fluid as defined in macroscopic voxels (averaging volumes) that surround each point of the porous material (a voxel, or volume element, is the 3D analog of a pixel, or picture element). Experimental advances in observing meniscus dynamics (e.g., Reynolds et al., 2017) and computational advances in pore-scale, interface-resolving methods (e.g., Abu-Al-Saud et al., 2017) demonstrate the complicated pore-scale interfacial dynamics occuring as immiscible fluids advance through a voxel. An ongoing challenge is to capture at the macroscopic scale the pertinent, averaged nature of the actual pore-scale physics during immiscible invasion.

The standard porous-continuum model of two-phase immiscible flow in an isotropic material involves two statements of mass conservation, where the index $i = w, n$ denotes either the wetting w or nonwetting n fluid,

$$\frac{\partial}{\partial t}[\phi S_i \rho_i] = -\nabla \cdot (\rho_i \boldsymbol{q}_i) \tag{2.1}$$

and two statements of momentum conservation that are written as Darcy transport laws

$$\boldsymbol{q}_i = k_o \frac{\kappa_i(S_w)}{\eta_i}(-\nabla P_i + \rho_i \boldsymbol{g}) \tag{2.2}$$

where ϕ is porosity, ρ_i average mass density of fluid i in a voxel, S_i saturation of fluid i (the volume of fluid i in a voxel divided by the volume of the pore space), $\boldsymbol{q}_i$ the Darcy velocity of fluid i (the average fluid i velocity relative to the solid framework of grains and multiplied by porosity), P_i the average fluid pressure in phase i, k_o the single-phase permeability of the material, and $\kappa_i(S_w)$ the dimensionless relative-permeability coefficients of each fluid, which are assumed to be functions of the saturation S_w.

Assuming that porosity remains constant during flow, once the Darcy laws are inserted into the two mass conservation equations, we have two equations for six unknowns: S_n, S_w, ρ_n, ρ_w, P_n and P_w. The remaining four equations are a statement that the pore space is entirely filled by both fluids

$$S_w + S_n = 1, \tag{2.3}$$

equations of state for each phase, which under isothermal flow conditions are the given monotonic functions $\rho_n(P_n)$ and $\rho_w(P_w)$, and, last, the assumption of a capillary-pressure function

$$P_n - P_w = P_c(S_w), \tag{2.4}$$

where $P_c(S_w)$ is a given monotonic function of saturation. The function $P_c(S_w)$ is typically measured experimentally under equilibrium hydrostatic conditions where S_w is changed slowly by small increments.

Our focus in this article is whether the above "standard model" of two-phase flow at the continuum scale, including commonly employed forms for the functions $\kappa_w(S_w)$, $\kappa_n(S_w)$ and $P_c(S_w)$, can capture the way that a gas invades a liquid-saturated porous material when the invasion is in the direction of the gravity field, which results in stable drainage fronts. Additionally, a requirement for the validity of Darcy's law in a given phase i is that the flow of phase i is laminar, which requires that phase i is continuous across each voxel. When a voxel is being drained for the first time prior to percolation, however, the nonwetting fluid is not continuous across the voxel. Also, it advances by discrete Haines jumps in which the local pressure drop across a meniscus trapped at a constriction in the pore space exceeds a threshold value, allowing the invading fluid to rush forward at relatively high Reynolds number (Re ~ 1) into downstream pores (Armstrong et al., 2015). At each jump, a single initial meniscus separates until all newly formed menisci become trapped at downstream capillary barriers, where they remain until the drainage causes the pressure drop across one of them to exceed the threshold value for that constriction, and another jump occurs. A Darcy law for the invading phase does not apply until percolation for that phase has occurred and laminar flow is taking place along the backbone of nonwetting fluid traversing the voxel. When saturation reaches a steady state, flow is laminar.

Formally, the relative permeability of the invading phase must be zero in a voxel undergoing invasion until the nonwetting saturation of that voxel reaches a critical value, S_{nc}, which corresponds to the nonwetting saturation at the moment of nonwetting-phase percolation across the voxel. In a macroscopic description of drainage, only once the nonwetting saturation is greater than S_{nc} can we begin to allow nonwetting fluid to invade the next downstream voxel according to the newly emergent Darcy's law. Here, we will show that S_{nc} is a function of the Bond (Bo) and capillary (Ca) numbers and the voxel size (L_z), and we will obtain an expression for the function $S_{nc}(\mathrm{Bo}, \mathrm{Ca}, L_z)$. During invasion, the defending wetting phase has a continuous path across the voxel and flows in a laminar manner between Haines jumps, as described by Darcy's law. The fractal nature of the invading fluid structure created in a voxel during the percolation process is incorporated into our model of S_{nc}.

The concept of achieving a critical saturation in a voxel prior to allowing nonwetting fluid to enter the next downstream voxel is not new. It was initially proposed by Corey (1954) and has been subsequently investigated by Dury et al. (1999), Yortsos et al. (2001) and Ghanbarian et al. (2016), among others. In particular, Dury et al. (1999) conclude: "an adequate description of the nonwetting phase relative permeability function by any model can only be expected if the emergence point of nonzero permeability is correctly represented."

We will show here that during drainage the one dimensional saturation profile $s(z)$ within a voxel depends on the buoyancy force as quantified by the Bond number (Bo), on the rate of invasion or extraction as quantified by the capillary number (Ca), and on the linear size of the voxel (L_z). We will also provide a model for the function $s(z)$ that is consistent with Invasion Percolation concepts.

Experiments conducted in bead monolayers and microchannel networks (e.g., Lenormand et al., 1988; Birovljev et al., 1991; Frette et al., 1997; Løvoll et al., 2005; Cottin et al., 2010; Toussaint et al., 2012; Hoogland et al., 2015) demonstrate that the morphology of a drainage front depends on the balance of buoyancy, viscous and capillary forces. The gravitational-pressure drop over a characteristic entry pore size a_0 in the direction $\hat{\mathbf{z}}$ of the average flow is given by $\Delta P_g = a_0 \hat{\mathbf{z}} \cdot \nabla P_g = a_0 \Delta\rho\, \hat{\mathbf{z}} \cdot \mathbf{g}$, where $\Delta\rho = \rho_w - \rho_n$ is the difference in fluid density and $\mathbf{g}$ the acceleration of gravity. Dividing this pressure drop by the capillary pressure drop across a meniscus γ/a_0, where γ is surface tension, defines the Bond number Bo

$$\mathrm{Bo} = \frac{a_0^2 \Delta\rho g\, \hat{\mathbf{z}} \cdot \hat{\mathbf{g}}}{\gamma}. \tag{2.5}$$

The viscous pressure drop over the pore distance a_0 in the direction of flow $\hat{\mathbf{z}}$ is given by $\Delta P_v = -a_0 \hat{\mathbf{z}} \cdot \nabla P_v = a_0 \eta_w \hat{\mathbf{z}} \cdot \mathbf{q}_w / k_o$, where η_w is the viscosity and $\mathbf{q}_w$ the interstitial velocity of the wetting fluid at the tip of the front. Dividing this viscous pressure drop by the capillary pressure drop across a meniscus defines the capillary number Ca

$$\mathrm{Ca} = \frac{a_0^2 \eta_w \hat{\mathbf{z}} \cdot \mathbf{q}_w}{\gamma k_o} \tag{2.6}$$

When Bo > 0, the drainage front is stabilized, and when Bo < 0, unstable gravitational fingers develop. For the drainage case where the invading nonwetting fluid is less viscous than the defending wetting fluid, even when Bo > 0, the tip of the invasion front becomes unstable when Ca becomes sufficiently large compared to Bo, resulting in viscous fingers of similar morphology to gravitational fingers (Glass et al., 2000).

Our work in this study is constrained by novel experimental measurements of gravity-stabilized drainage in a thin 3D bead pack. By continuously measuring light transmission across the thinnest dimension of the bead pack, we obtain 2D maps of how the saturation averaged over the thin width varies through time, and we compare these results to standard-model numerical simulations using TOUGH2 (Pruess, 2004) when the van Genuchten (1980) model for $P_c(S_w)$ has parameters determined experimentally for our specific flow cell. After demonstrating that the standard model does not accurately predict the observed saturation during invasion, the rest of the paper is dedicated to making modifications to the standard model based on the pore-scale physics of gravity-stabilized drainage at variable Bo and Ca.

Table 2.1: A table of symbols and notation, approximately in order of appearance.

S_w	wetting phase saturation []
S_{nw}	nonwetting phase saturation []
$\tilde{S}$	normalized saturation []
S_{nc}	critical nonwetting saturation []
S_{wc}	residual wetting saturation []
L_z	voxel length [L]
L_x, L_y	voxel lateral dimensions [L]
Bo	Bond number []
Ca	capillary number []

Continued on next page

Table 2.1 – *Continued from previous page*

Re	Reynolds number []
ϕ	porosity []
ρ	density [ML^{-3}]
$\boldsymbol{q}$	Darcy velocity [LT^{-1}]
k_o	permeability [L^2]
κ	relative permeability []
η	viscosity [ML$^{-1}T^{-1}$]
P	fluid pressure [ML$^{-1}T^{-2}$]
P_c	capillary pressure [ML$^{-1}T^{-2}$]
P_0	van Genuchten entry pressure [ML$^{-1}T^{-2}$]
a_0	characteristic pore size [L]
$\boldsymbol{g}$	acceleration of gravity [LT^{-2}]
γ	surface tension [MT^{-2}]
d_{50}	median grain size [L]
τ	light transmittance []
n	refractive index []
k	number of pores traversed by light []
I	light intensity [C]
I_o	intensity of the light source [C]
I_a,I_w	air (a) and water (w) -saturated light intensity [C]
$\tilde{I}$	normalized light intensity []
α	light absorption coefficient []
d_p	average pore diameter [L]
d_{cam}	image averaging height [L]
d_{width}	image averaging width [L]
λ	van Genuchten fitting parameter []
IP	Invasion Percolation
V_{nc}^{∞}	injected volume at percolation [L^3]
S_{nc}^{∞}	injected saturation at percolation []
D_c	fractal dimension []
d	Euclidean-space dimension []
N	number of lattice sites []
s	nonwetting saturation []
$w_o, \epsilon_1, \epsilon_2$	Bo = 0 $s(z)$ fit parameters
f_w	proportionality constant between s_w and S_{nc}^{∞} []
w	distance to inflection point in $s(z)$ [L]
s_w	nonwetting saturation at w []
h	distance to residual in $s(z)$ [L]
s_h	nonwetting saturation at h []
ξ	maximum cluster size in the defending phase [L]

Continued on next page

Table 2.1 – *Continued from previous page*

b_w	the slope of $s(z)$ at w [L^{-1}]
q	nonwetting phase occupation probability []
q_c	percolation threshold []
π	entry pressure distribution []
W_t	entry pressure distribution width []
ν	correlation length divergence exponent []
μ	$= \nu/(1+\nu)$ []
ℓ_w	proportionality constant in $w(\mathrm{Bo})$ [L]
$\mathrm{Bo_t}$	transitional Bo []
β_w	$s_w(\mathrm{Bo})$ exponent []
w_0	low Bo limit of w [L]
c_{sw}	proportionality constant in $s_w(\mathrm{Bo})$ []
s_{w0}	low Bo limit of s_w []
ω	$b_w(\mathrm{Bo})$ exponent []
c_{bw}	proportionality constant in $b_w(\mathrm{Bo})$ []
b_{w0}	low Bo limit of b_w [L^{-1}]
ℓ_ξ	proportionality constant in $\xi(\mathrm{Bo})$ [L]
a_h	characteristic wetting-saturated pore size at h [L]
μ_h	$h(\mathrm{Bo})$ exponent []
ℓ_h	proportionality constant in $h(\mathrm{Bo})$ [L]
s_{h0}	low Bo limit of s_h []
c_{sh}	fitting constant in $s_h(\mathrm{Bo})$ []
β_h	$s_h(\mathrm{Bo})$ exponent []
s_a	nonwetting saturation in the region $0 < z < w$ []
s_b	nonwetting saturation in the region $w \leq z \leq h$ []
f, f_1, f_2	curvature functions in s_b []
$\alpha_f, \beta_f, \delta_f, \tau_f$	fitting exponents in f, f_1, f_2 []
c_f, γ_f	constants in f_2 []
v_z	translational velocity of $s(z)$ profile [LT^{-1}]
z_o	position of lead menisci (leading tip of $s(z)$) [L]
A_w, A_ξ, A_{hw}, A_h	amplification factors controlling $s(z)$ distortion at nonzero Ca []
t_w	conductivity exponent []

2.3 Experiments and Associated Simulations

Laboratory Experiments

We perform drainage experiments in translucent, acrylic cells with dimensions 152 mm height, 76 mm width, and 13 mm thickness. The porous material is glass beads, screen size 20/30 (0.59 to 0.84 mm, $d_{50} = 0.72$ mm), similar to a coarse, well-sorted sand. We will characterize a typical entry pore size a_0 for the bead packs using $a_0 = d_{50}/3 = 0.24$ mm. Prior to assembly, a monolayer of beads is adhered to the inner walls of the cell with a clear, inert glue to prevent preferential flow along bead-wall interfaces. To exclude minor preferential flow in the corners of the cell and entry/exit effects, we record observations over a central region of 65 mm width x 115 mm height. Figure 2.1 shows the experimental setup and the inside of a flow cell.

We fill the cells by pouring beads rapidly through a randomizing screen to prevent continuous grain-size sorting. Once full, a vibration motor is attached to the cells and left running until the bead level stabilizes to 150 mm height, which produces a dense, stable, and repeatable packing.

Water flow into or out of the cell is regulated by a syringe pump connected to a manifold at the base. Prior to saturating with water, several pore volumes of CO_2 are passed through to displace air. The high solubility of CO_2 in water ensures that the chamber reaches full water saturation. Distilled water is then injected into the chamber at a slow flow rate, and porosity (ϕ) is calculated by measuring the water level several times during filling, yielding $\phi = 0.31$. Once full with water, the flow rate is slightly increased, and several pore volumes of water are passed through. The single-phase permeability (k_o) of the bead pack was measured by the falling head method, yielding $k_o = 1.6 \times 10^{-10}$ m^2. The air-water surface tension at laboratory temperature is $\gamma = 0.072$ Pa m.

Gravitationally-stable drainage ($\mathrm{Bo} = 7.4 \times 10^{-3}$) was performed by mounting the cell vertically and imposing a water withdrawal rate at the lower boundary with an atmospheric upper boundary. To observe any capillary number dependencies, a range of drainage flow rates was explored: 1 ml/min ($\mathrm{Ca} = 5.0 \times 10^{-5}$), 5 ml/min ($\mathrm{Ca} = 2.5 \times 10^{-4}$), 10 ml/min ($\mathrm{Ca} = 5.0 \times 10^{-4}$), 15 ml/min ($\mathrm{Ca} = 7.5 \times 10^{-4}$), 20 ml/min ($\mathrm{Ca} = 1.0 \times 10^{-3}$), 25 ml/min ($\mathrm{Ca} = 1.25 \times 10^{-3}$), and 30 ml/min ($\mathrm{Ca} = 1.5 \times 10^{-3}$). The largest flow rate corresponds to a Reynolds number of $\mathrm{Re} = \rho_\mathrm{w} \mathrm{a}_0 \mathrm{v}_\mathrm{w}/\eta_\mathrm{w} = 0.37$, which is close to the nonlinear advection regime ($\mathrm{Re} > 1$) where Darcy's law is invalid. Drainage timing begins when the first Haines jump occurs along the upper boundary. All observations were made on a single cell that was not repacked between drainage runs.

We measure saturation with visible light transmission. The light source is a diffused 7.5W LED panel. A monochrome video camera (Redlake Motionpro) is mounted 1 meter from the cell and captures images continuously. The amount of data that can be recorded during a drainage run is limited by the camera's internal buffer size. We maintain a constant 25 frames per second at a resolution of 17 pixels per centimeter in both dimensions. To relate measured light intensity I at a pixel to the average saturation S_w across the cell at that pixel,

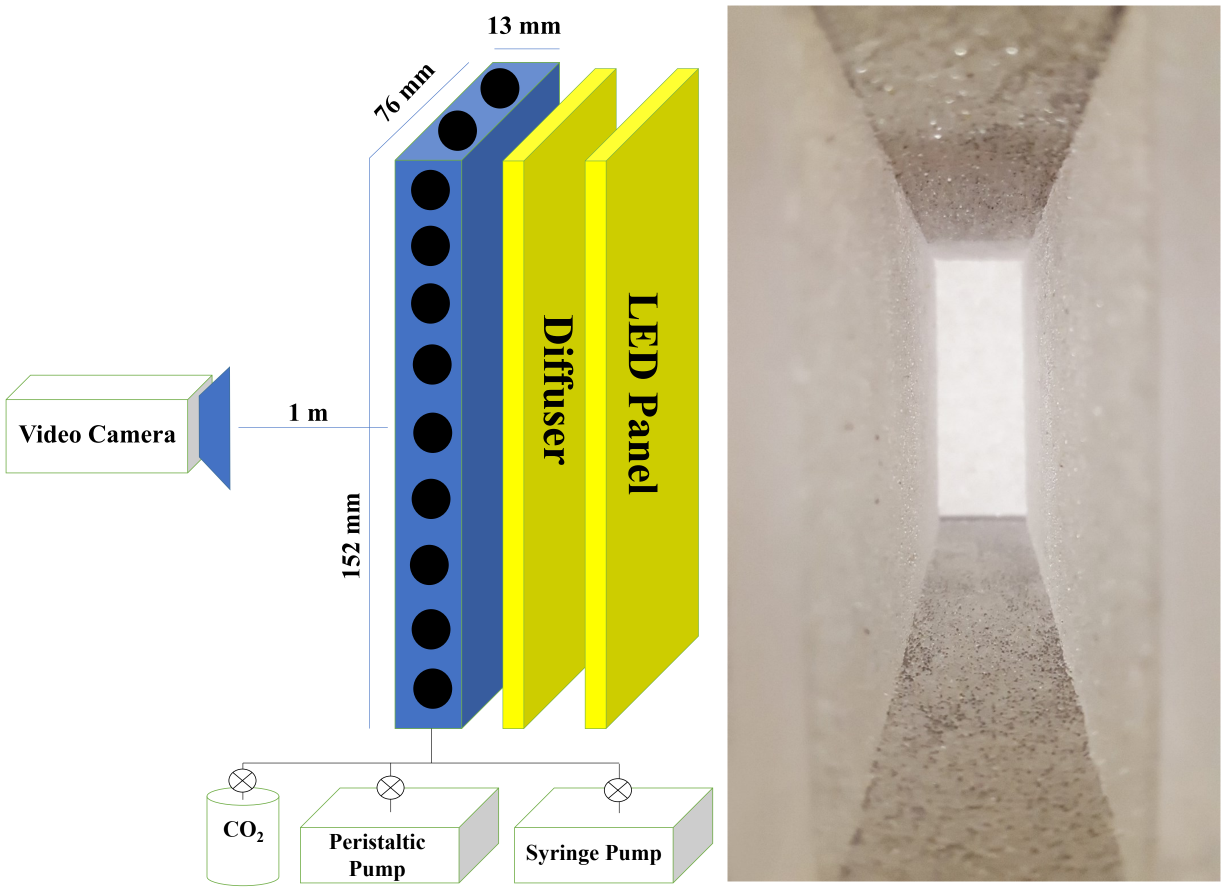

Figure 2.1: The experimental apparatus consists of a thin flow cell, a light diffuser, and a 7.5 W LED panel. A monochrome camera records continuously during drainage. A syringe pump is used to steadily withdraw fluid, and a peristaltic pump is used to saturate and flush the chamber with water after displacing air with CO_2. The photograph on the right shows the interior of the flow cell, which is lined with beads to minimize preferential flow along the inner walls.

the model of Tidwell and Glass (1994) fits our measurements quite well. Conceptually, if a beam of light of intensity I_o is incident on a layer of glass beads saturated with water and air, its intensity decreases by a transmittance factor each time it traverses from the solid beads into a pore and decreases exponentially with distance traveled in each phase due to absorption. The absorption coefficients in solid, air and water are denoted α_s, α_a and α_w.

The normal-incidence transmittance factor at a planar solid-air interface is

$$\tau_{sa} = \frac{4n_s/n_a}{(n_s/n_a + 1)^2} \tag{2.7}$$

where n_a is the refractive index of air ($n_a = 1.0$), and n_s is the refractive index of our glass beads ($n_s = 1.54$), which yields $\tau_{sa} = 0.955$. An identical expression exists for the transmittance factor τ_{sw} at a solid-water interface, which with $n_w = 1.33$ yields $\tau_{sw} = 0.991$. If there are an average of k pores traversed on a straight line across the cell such that $k_w = S_w k$ of them are saturated with water and $k_a = (1 - S_w)k$ are saturated with air, the distance traveled through water is $d_w = k_w d_p$, where $d_p \approx d_{50}$ is average pore diameter, the distance through air is $d_a = k_a d_p$, and the distance through solid is denoted d_s. Since each pore experiences two transmittances from solid to pore, we have the following model for the transmitted light intensity I:

$$I = I_o e^{-\alpha_s d_s - \alpha_w d_w - \alpha_a d_a} \tau_{sa}^{2k_a} \tau_{sw}^{2k_w}. \tag{2.8}$$

Defining I_a to be the transmitted intensity when $S_w = 0$ (fully air-saturated beads) and I_w to be the transmitted intensity when $S_w = 1$, we can rewrite the expression for I as

$$I = I_a e^{-(\alpha_w - \alpha_a) S_w k d_p} \left(\frac{\tau_{sw}}{\tau_{sa}} \right)^{2 S_w k}. \tag{2.9}$$

Assuming that $\alpha_w \approx \alpha_a$ and introducing the normalized intensity $\tilde{I}$ defined as

$$\tilde{I} = \frac{I - I_a}{I_w - I_a}, \tag{2.10}$$

these expressions can be inverted to obtain:

$$S_w = \frac{\ln\left(\tilde{I}\left[(\tau_{sw}/\tau_{sa})^{2k} - 1\right] + 1\right)}{2k \ln(\tau_{sw}/\tau_{sa})} \tag{2.11}$$

which is the Tidwell and Glass (1994) model. The normalized intensity $\tilde{I}$ consists entirely of measured quantities, while the parameter k is formally the number of pores across the system but is taken to be a fitting parameter. By measuring the average light intensity across all pixels covering our flow cell and fitting to the measured amount of water in the cell, we find that $k = 26$ fits the data best (Figure 2.2), which is larger, as expected, than a simple face-centered cubic estimate given by $k \approx 13$ mm $/d_{50} = 18$.

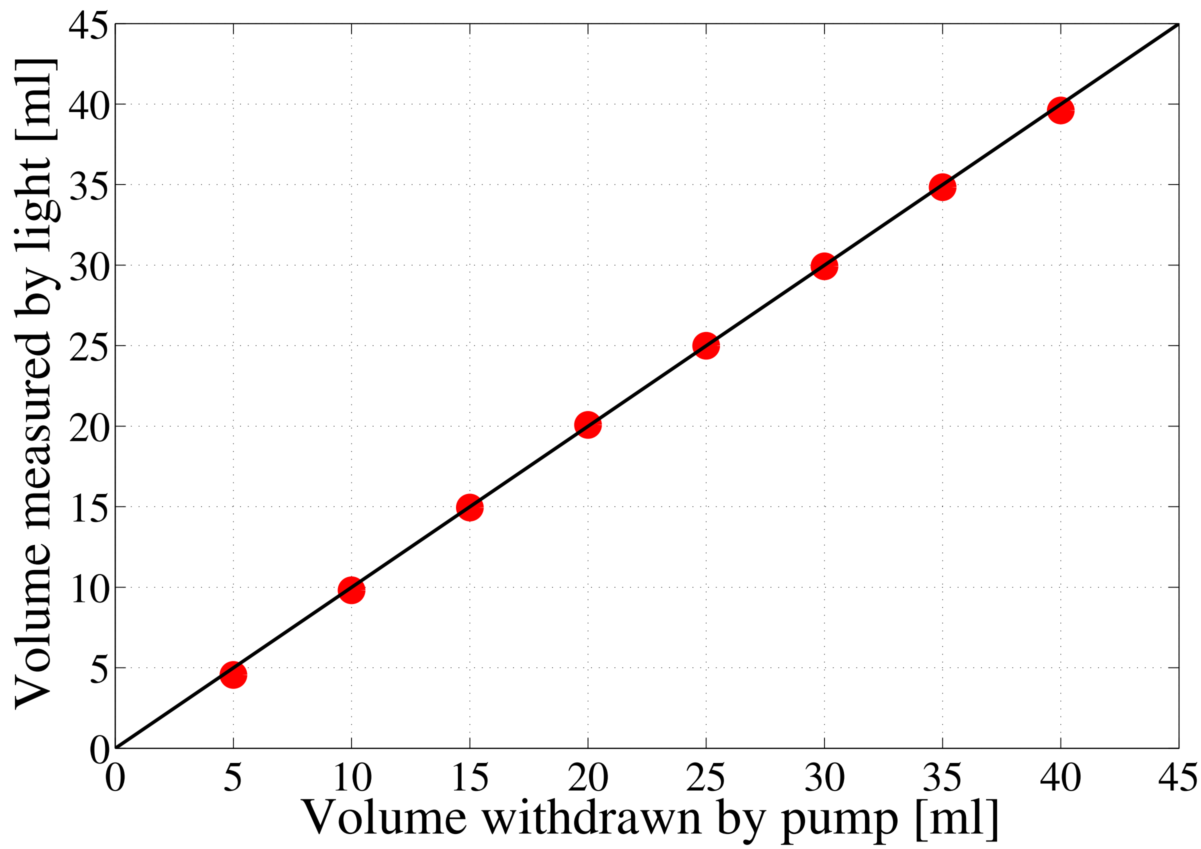

Figure 2.2: The volume of water in the cell as measured by light transmission is compared to the volume withdrawn by a syringe pump. The red dots are calculated by summation over 2D saturation images. The black line is 1:1, for reference.

Formally, the *Tidwell and Glass* model of Eq. (2.11) corresponds to taking the actual distribution of solid, air and water within the cell and redistributing these phases into $k_a = (1 - S_w)k$ layers of air embedded between layers of solid and $k_w = S_w k$ layers of water embedded between solid. This planar model for converting measurements of light intensity at a pixel into measures of water saturation across the width of the cell behind that pixel is clearly an approximation. The model will get worse as pixel size decreases relative to the size of the solid grains. For a face-centered cubic model, some light rays would pass nearly entirely through solid and others almost entirely through pores. The *Tidwell and Glass* model could not be expected to apply until enough transmitted rays passing through all combinations of solid, air and water are recorded on a rectangular patch of the cell. For our random packings, we will have all such rays represented on patches that are a few times larger than the average grain diameter. For our later purposes of comparing measurements to simulations, we measure saturation $s(z)$ as a function of height z in the cell by averaging the light intensity over rectangular patches that are one camera pixel high ($d_{\mathrm{cam}} = 0.59$ mm) at finest resolution and have widths given by $d_{\mathrm{width}} = 56$ mm wide. Even on such rectangular pixels at finest vertical resolution, all ray paths through the solid, air and water will be represented, and Eq. (2.11) is expected to apply. Because Eq. (2.11) is a nonlinear relation between $\tilde{I}$ and S_w, whenever a different patch size is used to determine saturation, one should in principle calculate the average values of all of I_a, I_w and I over the new patch size and then calculate the saturation behind the patch using Eqs. (2.10) and (2.11). Considering this, we performed saturation measurements at different resolutions both in this manner and by directly averaging the $s(z)$ function obtained first at camera resolution (i.e., on rectangular patches $d_{\mathrm{cam}} \times d_{\mathrm{width}}$), and the results are not significantly different.

Standard-Model Numerical Simulations

We test the standard model of drainage by performing 1D isothermal numerical simulations down the length of our cell using the TOUGH2, EOS3 code (Pruess, 2004) and comparing these results to experimental observations.

To accomplish this, the capillary-pressure curve used in the TOUGH2 simulations is first determined experimentally under static (non-flowing) equilibrium conditions. Water is drained from the cell slowly, until most of it has been invaded from above by air, and the equilibirum water saturation profile $S_w(z)$ above the phreatic surface $z = 0$ (controlled by an external reservoir) is measured optically when the cell reaches steady-state. Figure 2.3 shows the height z above the phreatic surface versus the measured static equilibrium water saturation $S_w(z)$ as measured on rectangular patches of size $d_{\mathrm{cam}} \times d_{\mathrm{width}}$. We fit this observation using the van Genuchten model

$$P_n - P_w = P_0(\tilde{S}^{-1/\lambda} - 1)^{1-\lambda} \tag{2.12}$$

where $\tilde{S}$ is the saturation normalized by residual saturation S_{wc} such that

$$\tilde{S} = \frac{S_w - S_{wc}}{1 - S_{wc}} \tag{2.13}$$

and where λ and P_0 are fit parameters. To convert $P_n - P_w$ into height z above the phreatic surface, we use the static equilibrium result that

$$P_n - P_w = \frac{\gamma}{a_0} + (\rho_w - \rho_a)gz \tag{2.14}$$

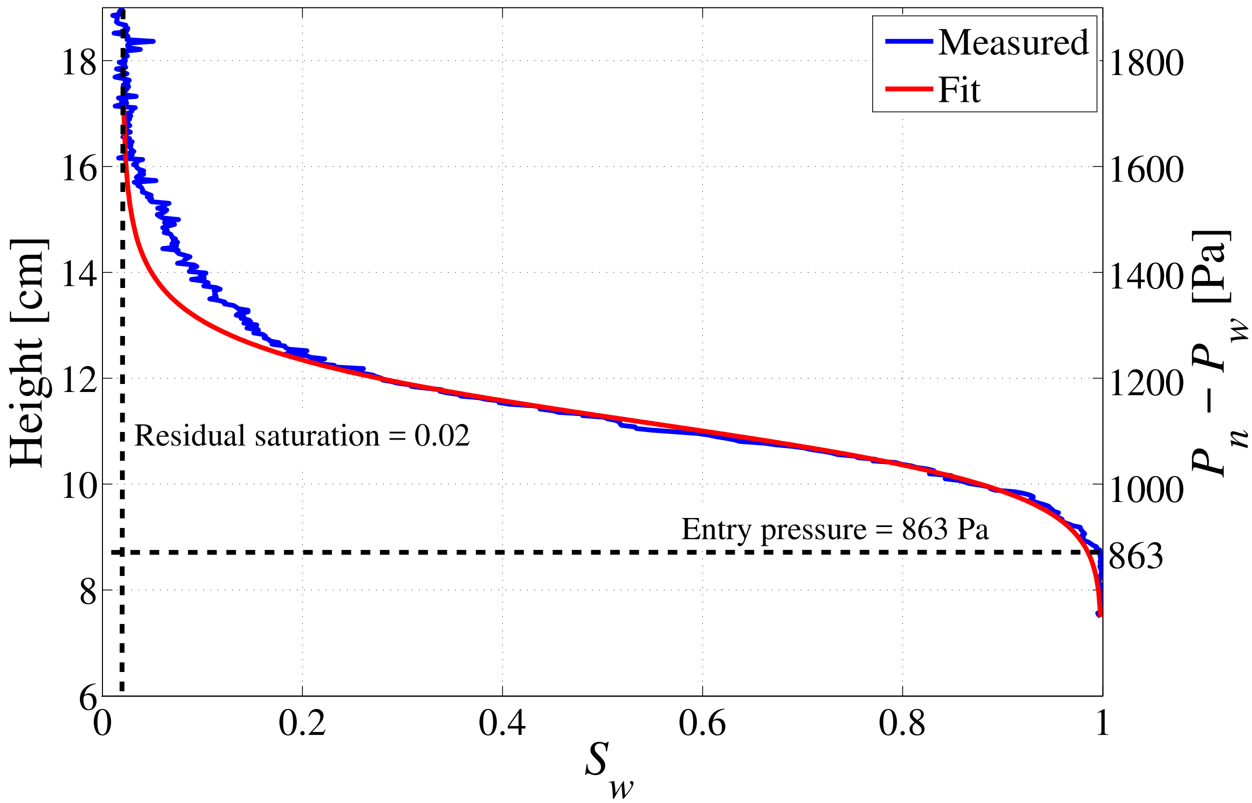

Figure 2.3: A steady-state saturation profile is measured optically (blue) as a function of height above the phreatic surface. The van Genuchten model (Eq. 2.12 with $\lambda = 0.94$ and $P_0 = 1100$ Pa) is fit to the observations. Note that the air entry pressure marked on the graph is not equivalent to the variable P_0.

where γ is the air-water surface tension, a_0 is the entry pore size (uniform from top to bottom in the cell), and γ/a_0 is the entry pressure for the porous material. Equating Eqs. (2.12) and (2.14) and using Eq. (2.13) gives a model for $S_w(z)$ that is shown as the red curve in Figure 2.3, with parameter values $\lambda = 0.94$ and $P_0 = 1100$ Pa. The fit is slightly inaccurate as residual saturation is approached higher in the cell. If H is the height of the cell, we expect that residual saturation will occur at a height $z = h < H$, where h scales with Bo and Ca, and that the capillary pressure will be a finite constant $\gamma/a_0 + (\rho_w - \rho_a)gh$ for all points $z > h$. In Figure 2.3, $h \approx 8$ cm.

The relative permeability of water used in the simulations is given by the van Genuchten–Mualem model, which uses the same λ as the capillary-pressure curve

$$\kappa_w = \begin{cases} \sqrt{\tilde{S}}[1 - (1 - [\tilde{S}]^{1/\lambda})^\lambda]^2 & \text{for } 0 \leq \tilde{S} \leq 1 \\ 0 & \text{for } \tilde{S} < 0. \end{cases} \tag{2.15}$$

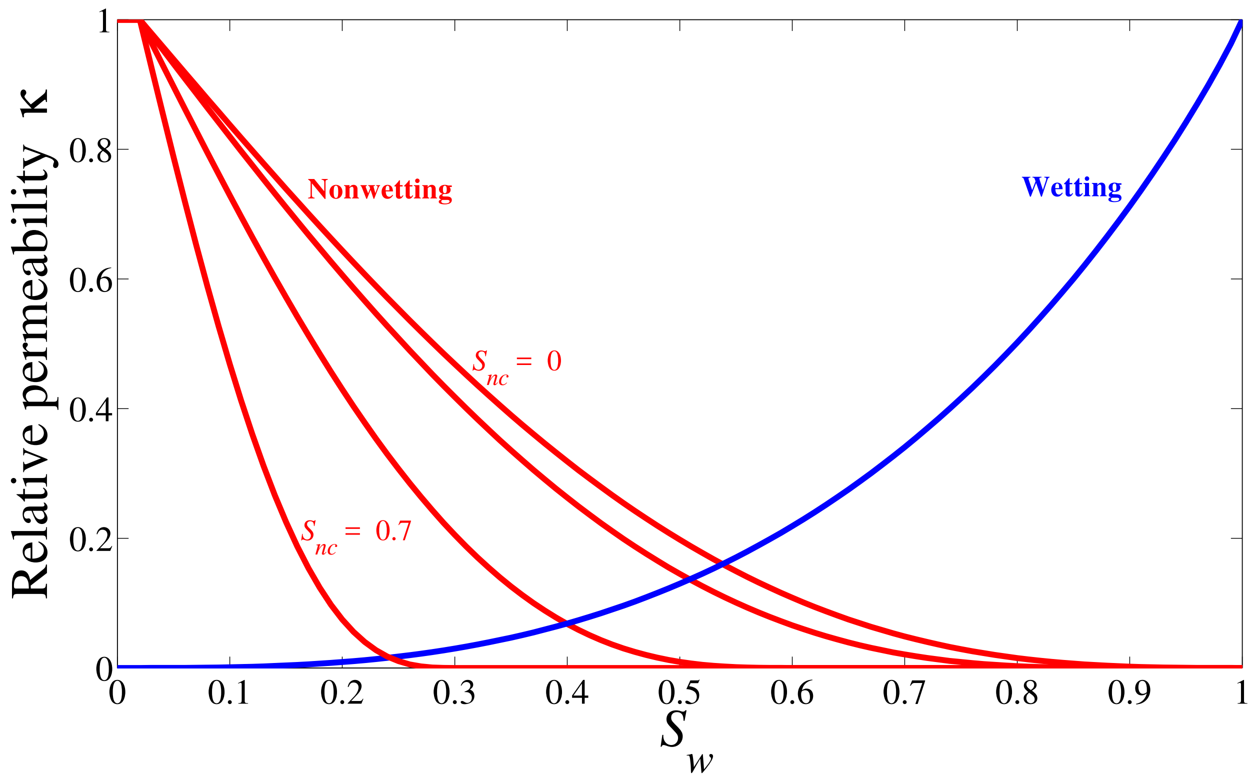

Figure 2.4: The relative permeability curves used in the numerical simulations are plotted. For the gas phase, we use the Corey model with a range of values for S_{nc}. For the water phase, we use the van Genucheten model with parameters taken from the fit to the static saturation profile.

The water's relative permeability has no free fit parameters (residual saturation S_{wc} is experimentally observed), and, conceptually, water is not allowed to flow if $S_w \leq S_{wc}$. In contrast, we use a Corey relative permeability curve for the air

$$\kappa_n = \begin{cases} (1-\hat{S})^2(1-\hat{S}^2) & \text{for } \hat{S} \leq 1 \\ 0 & \text{for } \hat{S} > 1 \end{cases} \tag{2.16}$$

where

$$\hat{S} = \frac{S_w - S_{wc}}{1 - S_{nc} - S_{wc}}. \tag{2.17}$$

Water saturation in the range $1 - S_{nc} \leq S_w \leq 1$ corresponds to $\hat{S} > 1$, which requires

$\kappa_n = 0$. This model for κ_n allows us to vary S_{nc} in the simulations. Figure 2.4 shows the corresponding relative permeability curves.

Finally, the initial condition for the simulations is full static water saturation. The upper boundary is maintained at atmospheric pressure, and the lower boundary has a constant water flux as imposed by the syringe pump. Because the side boundaries of the actual 3D cell have zero lateral flux conditions, the entire cell is reasonably modeled as a 1D, cell-length system. The discretization for the 1D simulations is a stack of 10 mm tall voxels, fifteen in all, implicitly having the same width and depth as the cell, with two boundary voxels at the top and bottom.

Comparing Experiments to Standard-Model Simulations

Figure 2.5 shows snapshots during drainage when gas begins to invade the bottom voxel of the field of study. The plotted comparisons are between the TOUGH2 simulations, the optically-measured saturation fields at the highest and lowest Ca, and hydrostatic conditions. Red horizontal lines denote the averaging voxels in the flow cell, which are also the simulation voxels. The grey images of optically determined saturation were determined on square pixels of size $d_{\mathrm{cam}} \times d_{\mathrm{cam}}$. The black dots marked "cell" in the graphs are the saturations optically determined by averaging light intensity over the rectangular patches that correspond to the simulation voxels (the red lines of size 10 mm $\times\, d_{\mathrm{width}}$). The red dots marked "simulation" are the standard model simulation results. The black line in the graphs are the optically-measured hydrostatic saturations, which are equivalent to Figure 2.3 but measured on patches of size $d_{\mathrm{cam}} \times d_{\mathrm{width}}$ resolution. The black round circles are the optically-measured hydrostatic saturations on the simulation voxels (10 mm $\times\, d_{\mathrm{width}}$).

The simulations (red dots) were performed using a van Genuchten model for $P_c(S_w)$ and $\kappa_w(S_w)$ that was fit to the measured equilibrium hydrostatic saturation profile according to standard practice. We obtain that for our voxel size $L_z = 10$ mm, the average S_{nc} is approximately 0.08 at Ca $= 5.0 \times 10^{-5}$ and 0.04 at Ca $= 1.5 \times 10^{-3}$. The fact that all parameters in the standard-model simulations were measured independently prior to the gas-invasion experiments and yet there remain significant differences between the simulation and optical measurements of saturation indicates that inappropriate assumptions are present in the standard model.

Figure 2.6 demonstrates how the parameter S_{nc} influences the air breakthrough time (i.e., the time for air to traverse the length of the field of study from the first Haines jump at the top to the final Haines jump that allows air to first touch the bottom boundary). In these simulations, we used the same S_{nc} for each of the 15 numerical voxels. Perhaps the most significant aspect of these results is that if $S_{nc} = 0$ for the gas phase, the simulated breakthrough time is 3.7 times faster than the observed breakthrough time. The simulated breakthrough times are influenced both by the capillary pressure function and the relative permeability functions for each phase. The general trend that increasing S_{nc} slows down simulated breakthrough times is expected because higher S_{nc} requires more air to enter each voxel before desaturating the next one downstream. However, the result that the best S_{nc}

for predicting breakthrough times at Ca $= 1.5 \times 10^{-3}$ is roughly 0.72, while the optically measured S_{nc} at this capillary number and voxel size is 0.08, may be a result of using the improper equilibrium $P_c(S_w)$ relation at high capillary number, as well as the fact that the van Genuchten (1980) model for $P_c(S_w)$ is problematic in the range of $1 - S_{nc} < S_w < 1$. How rapidly an individual simulation voxel achieves S_{nc} is strongly influenced both by the $P_c(S_w)$ function for that voxel in the range $1 - S_{nc} < S_w < 1$ and by the influence of the relative permeability model on pressure gradients.

The main conclusion of the present section, in which laboratory measurements of saturation in a flow cell have been compared to numerical simulations based on the standard model of two-phase flow with all free parameters independently measured, is that the standard model does not adequately reproduce the experimentally observed drainage profiles. Two key features are missing from the standard model: (1) rules for how S_w varies in each voxel as it is being invaded for the first time, based on the physics of gravity-stabilized drainage; and (2) once a voxel percolates with gas at $S_w \leq 1 - S_{nc}$, new models for $P_c(S_w)$, $\kappa_w(S_w)$ and $\kappa_n(S_w)$ must be used, with dependence on Ca, as first illustrated in Figure 2.5, and with dependencies on Bo and L_z as demonstrated in the following sections. Overall, the standard model can only apply to voxels where both fluid phases percolate and does not address the actual capillary physics and associated saturation structures occurring in those voxels that are being actively invaded for the first time.

2.4 Saturation Models for Stable Invasion

To incorporate Bo and Ca into models for S_{nc} and, more broadly, into models for how saturation varies behind the invasion front, we turn to percolation theory. Most of our analysis will be motivated by the Wilkinson (1984) Invasion Percolation (IP) algorithm in the presence of a buoyancy force and finite viscous flow. Our first goal is to obtain models for how nonwetting saturation varies with distance behind the front, which will allow us to determine the dependencies within a $S_{nc}(\mathrm{Bo}, \mathrm{Ca}, L_z)$ function.

In what follows, we will not rederive all needed IP scaling results from the literature but will attempt to describe in words the physics involved. Further, several of the scalings have exponents that we take from numerical simulations of IP, and the models that follow are therefore not built entirely from theoretical analysis and are meant only to capture the scalings and trends observed in the laboratory measurements and IP numerical simulations.

Saturation Model when $\mathrm{Bo} = 0$ and $\mathrm{Ca} \approx 0$

Consider first that gravity is not present and that the invading fluid is moving slowly enough for the Invasion Percolation algorithm of Wilkinson and Willemsen (1983) to be valid. The condition for Invasion Percolation to be a realistic model is that the viscosity-controlled pressure drop across a voxel of length L_z is small compared to the capillary pressure drop

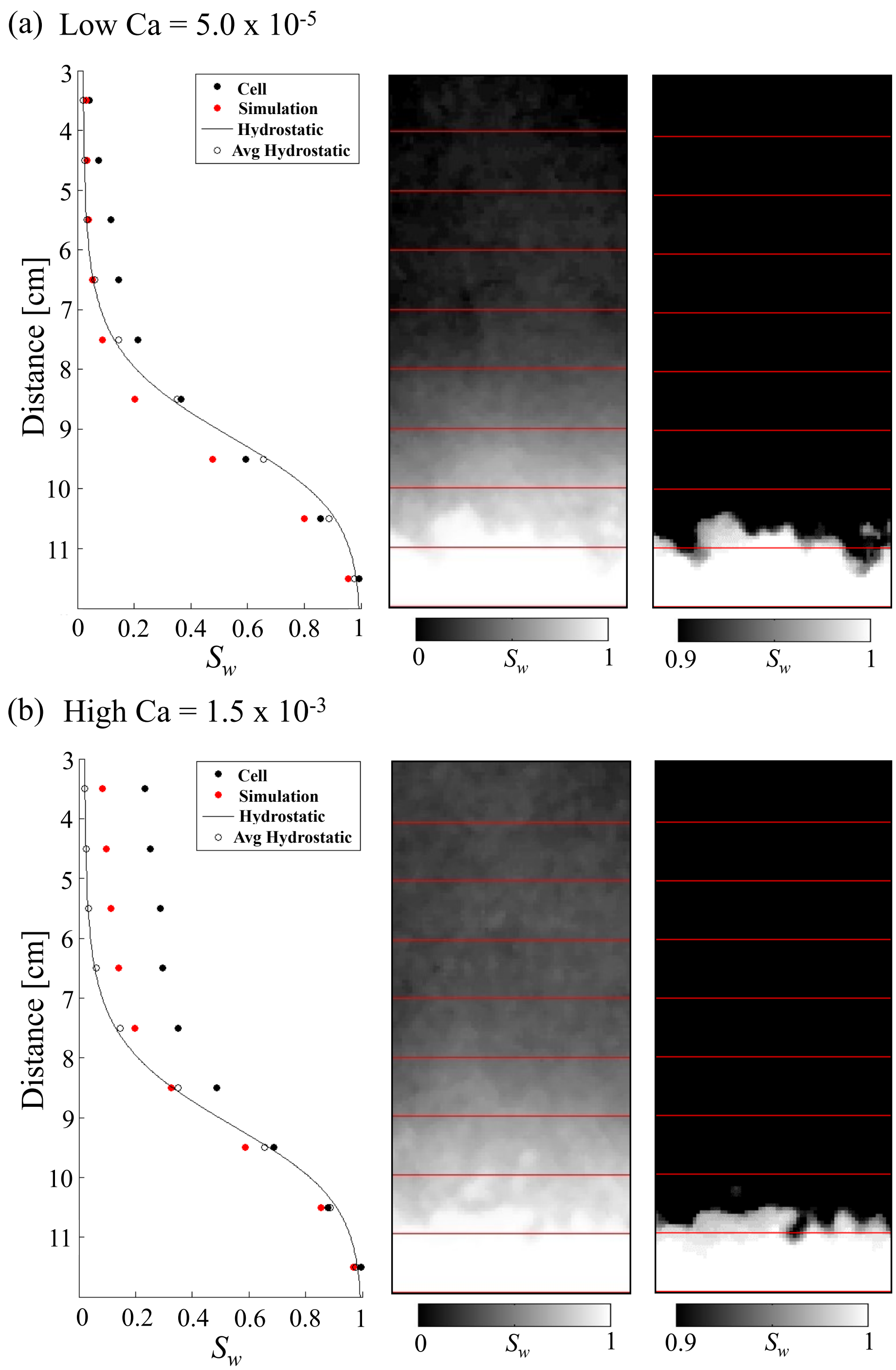

Figure 2.5: S_w observations from experiments at low (a) and high (b) Ca are shown. The 2D S_w images at center and right use different grayscale thresholds to highlight upstream and frontal regions, respectively. On the left, saturation is scaled up to the voxel size (red rectangles on the 2D S_w images) and plotted alongside simulations, with hydrostatic curves from Figure 2.3 to help visualize flow-induced stretching of the saturation curve. The saturation plots on the left are vertically aligned with the 2D S_w images.

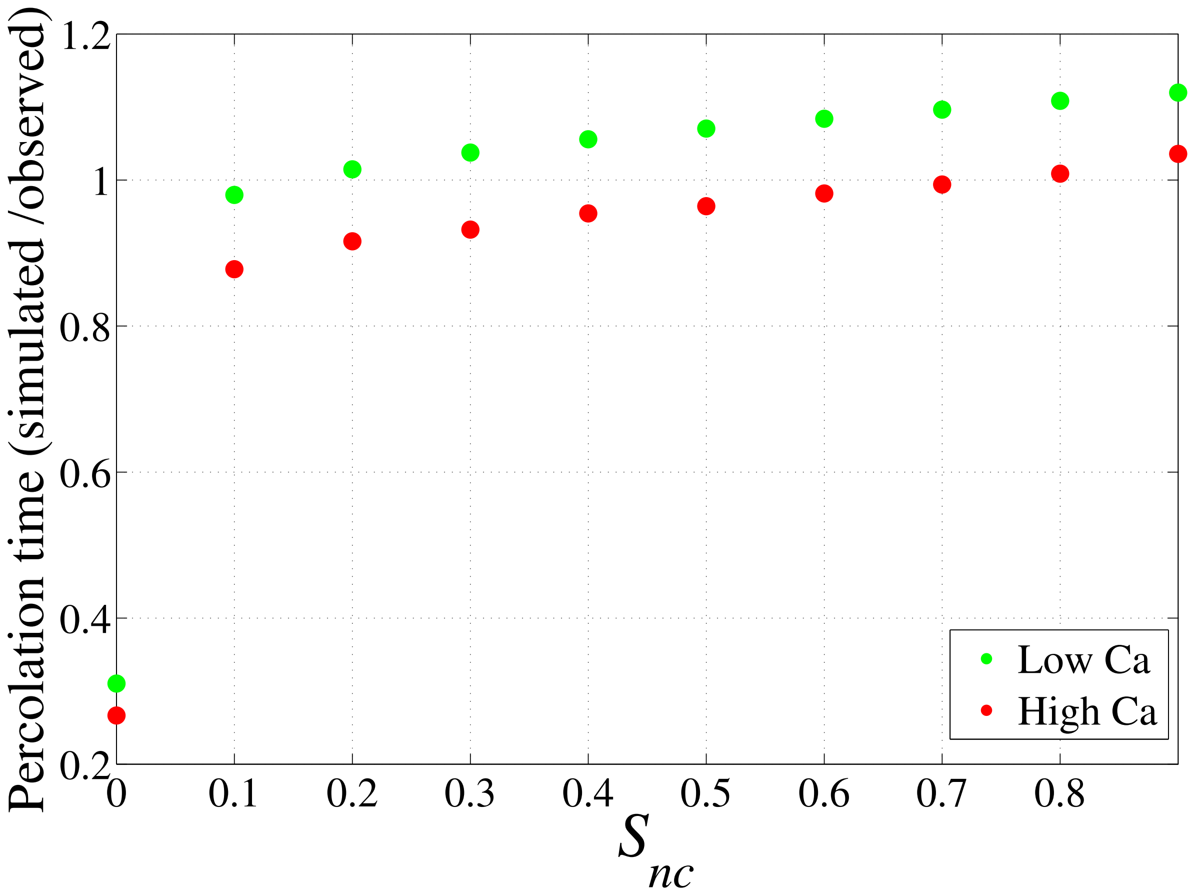

Figure 2.6: Percolation times indicate that finite values of S_{nc} can cause approximately fifteen percent variability in front speed, while $S_{nc} = 0$ allows a thin finger of air to propagate very quickly. To match observed front speed, artificially high and Ca-dependent S_{nc} values are needed.

across a meniscus residing in an entry pore of radius a_0, which corresponds to the condition that $\mathrm{Ca} \ll a_0/L_z$.

If the voxel has lengths L_x and L_y (both $> L_z$) in the lateral directions, we divide the voxel into cubes of volume L_z^3, so that there will be $L_xL_yL_z/L_z^3 = L_xL_y/L_z^2$ such cubes in the voxel. In this case, the critical volume of injected fluid at percolation within a large invasion cluster is a fractal given by (Wilkinson and Willemsen, 1983)

$$V_{nc}^{\infty} = \phi a_0^3 \left(\frac{L_z}{a_0}\right)^{D_c} \frac{L_xL_y}{L_z^2} \tag{2.18}$$

where ϕ is the porosity of the material, and D_c is the fractal dimension for ordinary capillary fingering without the influence of pressure gradients, which in a 3D cubic lattice has the universal value $D_c = 2.52$ (and $D_c = 91/48 = 1.90$ in 2D). This result holds for the infinite cluster that is sampled in sufficiently large systems, as denoted by the superscript ∞. The subscript n again denotes nonwetting, while subscript c denotes the critical threshold at percolation.

The saturation associated with the invaded volume V_{nc}^{∞} is found by dividing by the total pore volume $\phi L_x L_y L_z$

$$S_{nc}^{\infty} = \frac{V_{nc}^{\infty}}{\phi L_x L_y L_z} = \left(\frac{L_z}{a_0}\right)^{(D_c - d)} \tag{2.19}$$

where d is the Euclidean-space dimension of the system. Because $D_c - d$ is negative, the saturation of invading nonwetting fluid at breakthrough is a decreasing function of the size of the voxel in the direction of flow. Note that if the smallest system (voxel) dimension was L_x and not L_z, then the above argument would repeat by paving the saturation structure with cubes of volume L_x^d, resulting in $S_{nc}^{\infty} = (L_x/a_0)^{D_c - d}$.

Such slow invasion when $\mathrm{Bo} = 0$ can begin to occur once the applied capillary pressure $P_c = P_n - P_w$ exceeds a threshold given by $P_c \geq \gamma/a_0$. From the macroscopic porous-continuum perspective, in which the fluid pressure fluctuations due to Haines jumps are not detected, as long as each voxel has the same a_0, the slow invasion will proceed with P_c uniform and with both fluids percolating across all invaded voxels. To view the emergent nonwetting saturation profile $s(z)$ for invasion occurring in the $-z$ direction (with $z = 0$ defining the tip of the invasion cluster), we use the fast Invasion Percolation algorithm of Masson (2016) which allows for trapping. Simulation is performed on a 3D system of size $N_x = 400$, $N_y = 400$, and $N_z = 1600$ that has periodic boundary conditions in the x and y direction with injection occurring from all points of the face $z = N_z$. For this scenario, the limiting (maximum) saturation along $s(z)$ associated with the infinite cluster is given by $S_{nc}^{\infty} = N_x^{D_c - d} = (400)^{-0.48} = 0.06$, which holds for large enough z.

In Figure 2.7 we plot the saturation profile $s(z)$ obtained using the IP simulation as well as the expression

$$s(z) = S_{nc}^{\infty} \frac{(z/w_o)^{\epsilon_1 \epsilon_2}}{[1 + (z/w_o)^{\epsilon_1}]^{\epsilon_2}} \tag{2.20}$$

with fit parameters $w_o = 122$, $\epsilon_1 = 1.2$, and $\epsilon_2 = 2.1$. This form is purely empirical and was chosen to match the sigmoidal shape that tends to the constant theoretical value of $s_{nc}^{\infty} = N_x^{D_c - d}$ after passing through the inflection at $z = w$, where w is measured to be $w = 89.7$ for the given fit parameters. The saturation at the inflection point s_w which is

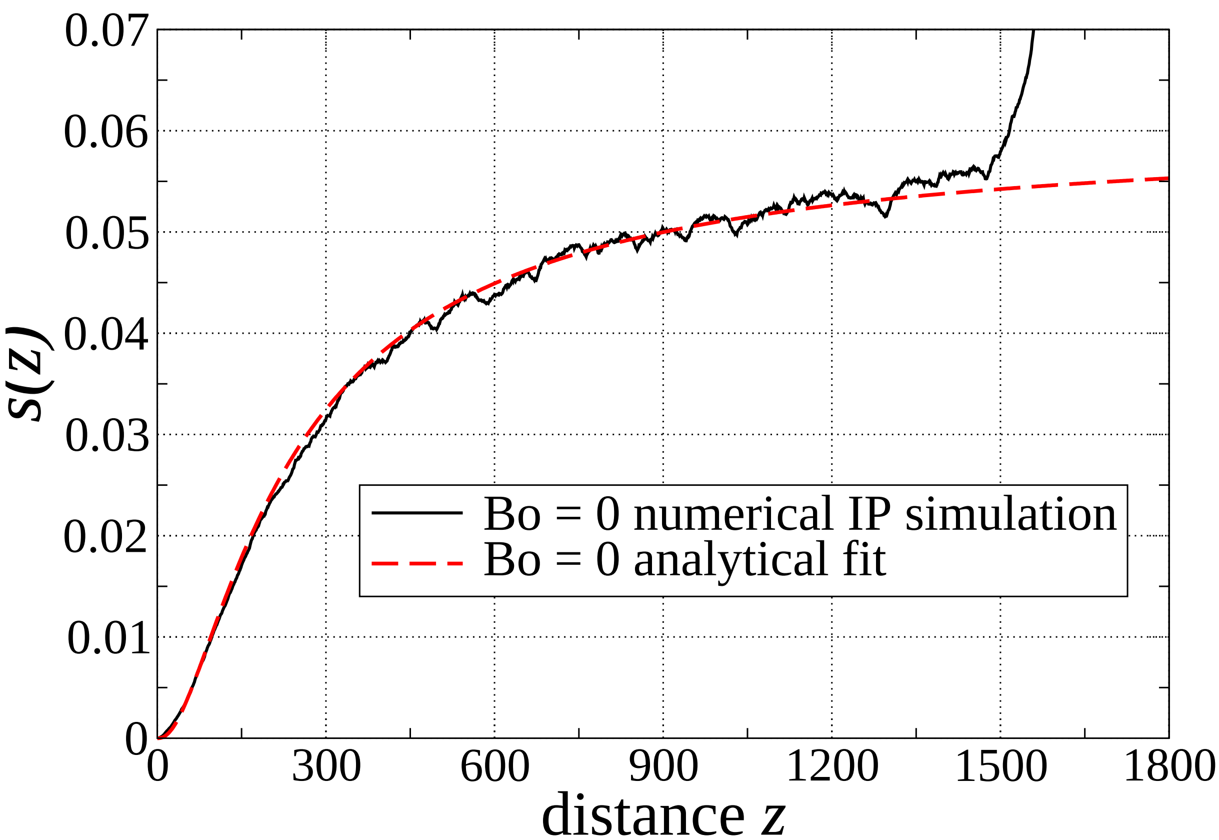

Figure 2.7: IP simulation at Bo $= 0$ of the saturation profile $s(z)$ of an IP invasion cluster with $z = 0$ at the tip, and the injection face at $z = 1600$. Total system size was $400 \times 400 \times 1600$. The saturation state is perturbed by the injection boundary for a distance of roughly 100 lattice points. The dashed curve is the function of Eq. (2.20).

needed later is thus

$$s_w = f_w S_{nc}^{\infty} \tag{2.21}$$

where the parameter f_w is defined

$$f_w = \frac{(w/w_o)^{\epsilon_1 \epsilon_2}}{[1 + (w/w_o)^{\epsilon_1}]^{\epsilon_2}} \tag{2.22}$$

where $w/w_o \approx 0.74$ and $f_w \approx 0.15$.

In a finite system of size L_z, the saturation of nonwetting fluid at percolation is

$$S_{nc} = \frac{1}{L_z} \int_0^{L_z} s(z)\, dz. \tag{2.23}$$

We then have $\lim_{L_z \to \infty} S_{nc} \to S_{nc}^{\infty}$ in a sufficiently large system where the saturation near the injection boundary and the fall off in saturation toward the invasion tip do not occupy a significant fraction of the total system volume.

Saturation Model when $\mathrm{Bo} > 0$ and $\mathrm{Ca} \approx 0$

Wilkinson (1984) defines a variant of Invasion Percolation that incorporates variable P_c due to gravity (IP in a gradient field) when the invasion is again occurring so slowly that viscosity may be neglected.

If Bo is positive (e.g., air invading water in the direction of gravity), the invasion front is stabilized; i.e., long fingers of invading fluid do not develop and, further, the region over which both phases percolate behind the front becomes compressed compared to when gravity does not act. For a gas invading a liquid (drainage) with $\mathrm{Bo} > 0$, downward gas jumps in the direction of gravity are somewhat less favored due to the increasing liquid pressure compared to horizontal jumps, with the result that trapped clusters of defending fluid develop even in 3D. However, if $\mathrm{Bo} < 0$ (e.g., air invading water against the gravity field), unstable gravitational fingers develop because upward gas jumps are favored relative to horizontal jumps due to the decreasing liquid pressure with upward distance.

For stable gas invasion in the direction of gravity, the Wilkinson (1984) model of IP results in a transition layer of thickness h behind the lead menisci (which we continue to define as being located at $z = 0$) that separates the capillary fingering occurring in the frontal region from a constant, statistically homogeneous "residual saturation" region well behind the front. Across the region $0 < z < h$ behind the front, in 3D, both phases form connected paths. Above this region (i.e., $z > h$), the liquid is below the percolation threshold, the capillary pressure is at a maximum, and all parts of the pore space originally occupied by liquid that can be invaded by gas have already been invaded. Any remaining liquid is in disconnected clusters of maximum size ξ that corresponds to the correlation length in the defending liquid. As gas flows through this residual-saturation region to get to the advancing menisci at the front, no further jumps or changes to the saturation state occur. The liquid does not flow in the residual-saturation region. In addition, near the front where the gas phase first percolates at $z = 0$, we can define a second correlation length w within the gas phase that effectively defines the width of the random capillary-fingering region occurring immediately behind the front.

At the position of the lead miniscii ($z = 0$) there are capillary fingers probing the porous material for the smallest capillary-pressure threshold to invade next. This random capillary-fingering structure immediately behind the lead menisci ($0 \le z \le w$) transitions after an

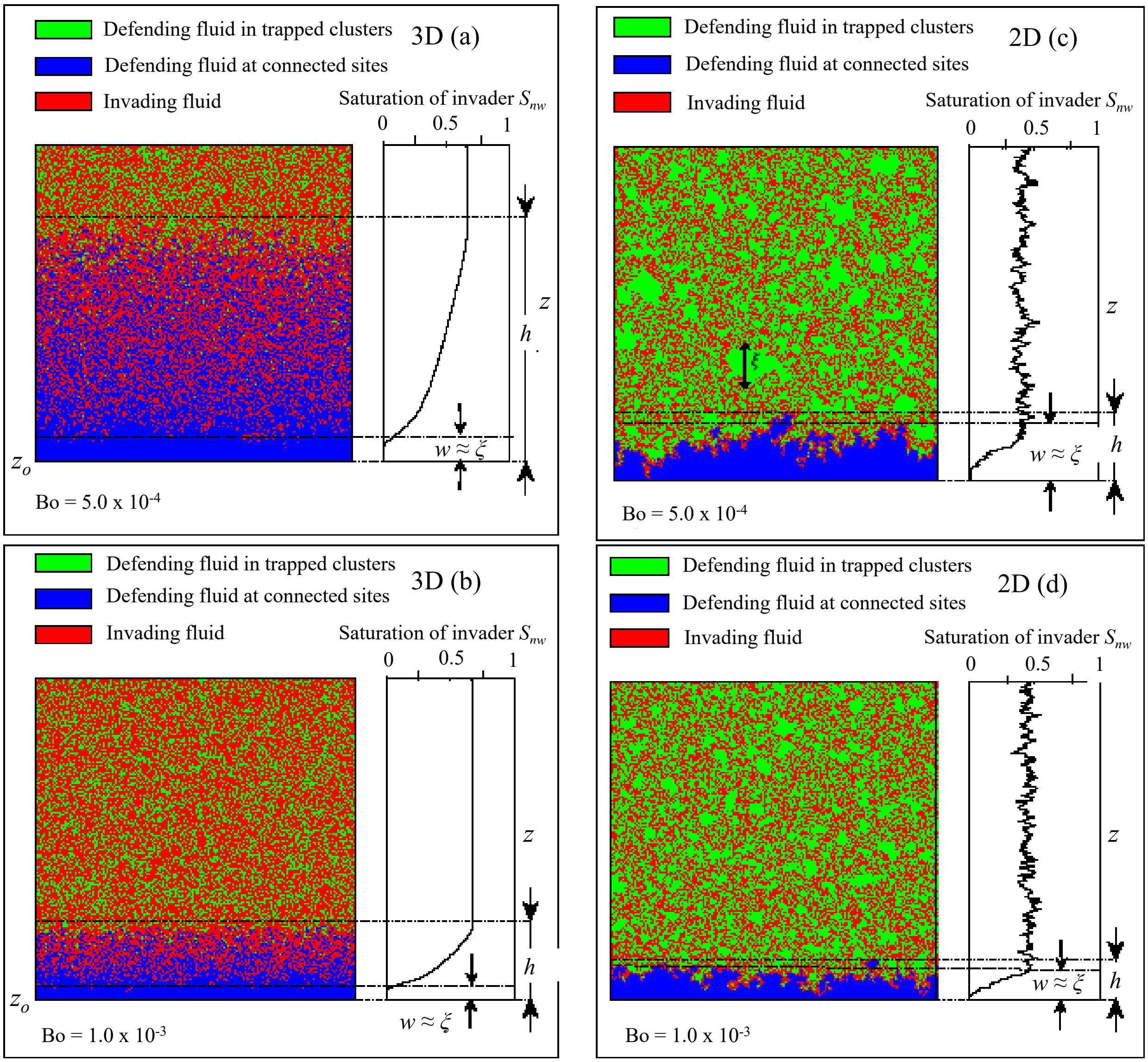

Figure 2.8: Snapshots of IP numerical results both in 3D (column on left) and 2D (column on right) at the moment of percolation. In 3D, each vertical slice is through the middle of the $400 \times 400 \times 400$ system. In all panels, the red fluid invades from the top surface to the bottom. The length h between the front tip and the point where the defending fluid is entirely disconnected into isolated clusters is measured numerically on the entire 3D system, not just on the slices shown in (a) and (b). The front width w was measured numerically as the inflection point in the saturation profile and corresponds to the scaling of Eq. (2.28). The maximum trapped cluster size is the same as the front width ($\xi = w$) when viscous pressure gradients can be neglected. In 3D, the lengths $\xi = w$ and h are distinct and have different scalings with Bo, while in 2D we observe $\xi = w \approx h$. Also, in 3D the residual saturation of the defending phase is much lower than in 2D, and ξ is smaller.

inflection point at $z = w$ into the region ($w \leq z \leq h$) where the increasing capillary pressure with increasing z is causing defending fluid to become pinched off in places until for distances $z > h$ the defending fluid is entirely disconnected into patches having maximum size ξ.

The three lengths w, ξ and h can be viewed in the numerical snapshots of the saturation distribution shown in Figure 2.8. These were made with the Invasion Percolation algorithm of Masson (2016) on a $400 \times 400 \times 400$ point grid in 3D and 400×400 in 2D. The simulations are of a lighter fluid like air slowly invading downward (in the direction of gravity) into a denser defending fluid like water. In 2D, all three lengths are equivalent $w \approx \xi \approx h$, while in 3D with a uniform gravitational pressure gradient, we have $w \approx \xi < h$. When variable viscous pressure gradients are present, as considered later, in 3D we will have $w < \xi < h$. Note that the definition of front width, w, in 3D is the inflection point of the $s(z)$ curve, while in 2D it is the maximum separation distance in z of the lead menisci.

A major goal of this work is to obtain an expression for the invading-fluid saturation profile $s(z)$. There are five key observables that scale with Bo and serve as anchor values for the $s(z)$ profiles. These are: (1) the width $w(\text{Bo})$ of the capillary-fingering region immediately behind the front; (2) the invading fluid's saturation $s_w(\text{Bo})$ at $z = w$; (3) the slope of the saturation profile at $z = w$ defined as $b_w(\text{Bo}) = \mathrm{ds(z)/dz}|_{\mathrm{z=w}}$; (4) the width $h(\text{Bo})$ of the entire dual-percolation zone; and (5) the saturation $s_h(\text{Bo})$ at $z = h$. Additionally, we require that at $z = h$, the slope is zero $ds(z)/dz = 0$, and the curvature is negative $d^2s(z)/dz^2 < 0$. We now go on to obtain the scaling laws for these five observables and then propose functional forms for the profile $s(z)$ that are anchored by these values.

Observables at the front: w, s_w and b_w

A first step is to establish how the width w of the frontal region scales with Bo. The argument is similar to that for how the maximum length ξ of the residual-water clusters depends on Bo. All of Wilkinson (1984), Rosso et al. (1985), Birovljev et al. (1991), and Méheust et al. (2002) derive the scaling for ξ, and we follow a similar argument for w here. The width of the front w can be interpreted as a correlation length in the invading gas phase and addressed with ideas from ordinary percolation. Let q be the allowed occupation probability of the invading gas within voxels behind the front. This is formally distinct from the gas saturation because not all pores initially filled with water can be invaded if that water is trapped (i.e., surrounded by gas), while the definition of q allows for all water-filled pores to potentially be invaded by gas if the local capillary pressure exceeds the entry threshold of the water-filled pore. At the lead voxel just behind the front $z = 0$, there is a percolation threshold q_c that occurs at the capillary entry pressure $P_c(z = 0) = \gamma/a_0$ for that voxel. The relation for the occupation probabilities $q(z)$ at a distance z behind the front can be written

$$q(z) - q_c = \int_{P_c(0)}^{P_c(z)} \pi(P)\, dP \tag{2.24}$$

where $P = \gamma/a$ is the threshold capillary pressure for air to enter a water-saturated pore of size a, and $\pi(P)$ is the probability distribution for these thresholds. If $\pi(P)$ is relatively flat with width $W_t = \gamma(1/a_{\min} - 1/a_{\max})$, we can approximate $\pi(P) \approx 1/W_t$ and write

$$q(z) - q_c = \frac{P_c(z) - P_c(0)}{W_t} = \frac{1}{W_t}\int_0^z \frac{\partial P_c(z')}{\partial z'}\,dz'. \tag{2.25}$$

We can then define a correlation length w from the usual percolation definition $w \propto [q(w) - q_c]^{-\nu}$ or

$$\frac{w}{a_0} = \text{const}\left(\frac{1}{W_t}\int_0^w \frac{\partial P_c(z')}{\partial z'}\,dz'\right)^{-\nu} \tag{2.26}$$

$$= \text{const}\left(\frac{a_0}{W_t}\frac{1}{w}\int_0^w \frac{\partial P_c(z')}{\partial z'}\,dz'\right)^{-\nu/(1+\nu)} \tag{2.27}$$

where $\nu = 0.875$ in 3D (and 4/3 in 2D). We finally rewrite this as

$$w = \ell_w\left(\frac{a_0^2}{\gamma}\,\frac{1}{w}\int_0^w \frac{\partial P_c(z')}{\partial z'}\,dz'\right)^{-\mu} \tag{2.28}$$

where $\mu = \nu/(1+\nu) = 0.47$ in 3D (and 0.57 in 2D), and the pressure-independent length

$$\ell_w = \text{const}\ a_0\left(\frac{a_0 W_t}{\gamma}\right)^{\mu} \tag{2.29}$$

is adjusted to fit data. The dimensionless quantity a_0W_t/γ only depends on the pore size distribution. Equation (2.28) for w is valid even if the capillary pressure gradient is variable behind the front, as it will be at finite wetting-phase velocity.

At small rates of extraction defined by $\mathrm{Ca} \ll \mathrm{a_0/L_z}$, the capillary pressure gradient is due to gravity alone, which is uniform in space. In this case, Eq. (2.28) becomes

$$w = \ell_w \mathrm{Bo}^{-\mu}. \tag{2.30}$$

To test this prediction, we use the fast algorithm of Masson (2016) for Invasion Percolation in a gradient to perform numerical simulations on systems of size $N_x \times N_y \times N_z$. Our flow-cell experiments, when measured in lattice units corresponding to the average distance between two pores, constitute a system size of $N_x = 18$, $N_y = 105$ and $N_z = 212$, which we use in

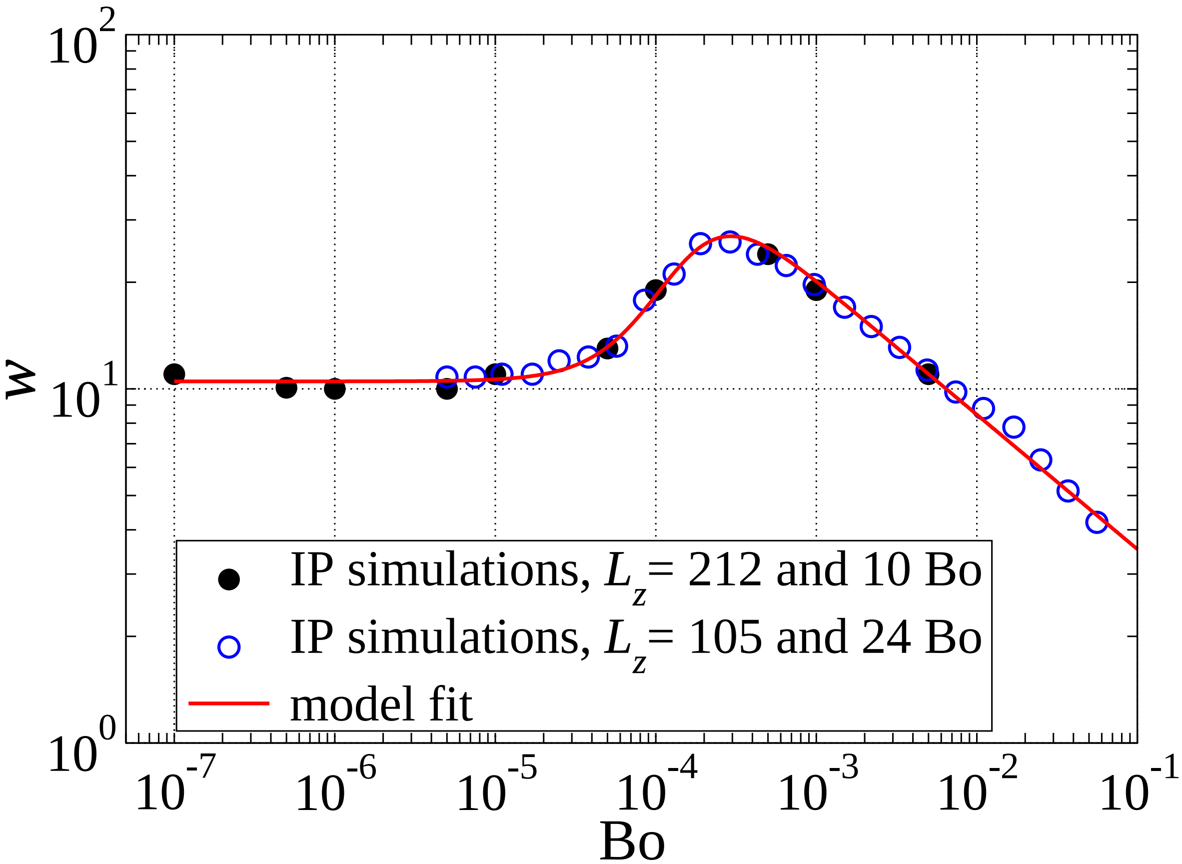

Figure 2.9: Numerical measurements of the inflection point w as a function of Bo (measured in lattice units using the fast IP algorithm of Masson (2016) that does not invade trapped clusters). The model fit corresponds to Eq. (2.31). The simulation domain has dimensions (measured in lattice units) of $18 \times 105 \times L_z$. Two different L_z were considered: $L_z = 212$ (with 10 different Bo) and $L_z = 105$ (with 24 different Bo).

the numerical experiments.

To measure w numerically, we define it as the inflection point in the nonwetting saturation profile $s(z)$. For each Bo, we generate numerically an IP nonwetting saturation curve $s(z)$ at the moment that the nonwetting invading fluid first percolates the system. By taking a derivative $ds(z)/dz$ and identifying $z = w$ as the point where the derivative is maximized, we obtain the front width w for each Bo, as well as the corresponding saturation $s_w = s(w)$ and the maximum slope $b_w = ds(z)/dz|_{z=w}$ at the point $z = w$. The results are plotted in Figures 2.9, 2.10 and 2.11.

Figure 2.9 shows that although at large Bo there is indeed the predicted power-law relation of $w = \ell_w \mathrm{Bo}^{-\mu}$ with $\mu = 0.47$ (3D), there is a transition to the constant w_0 for

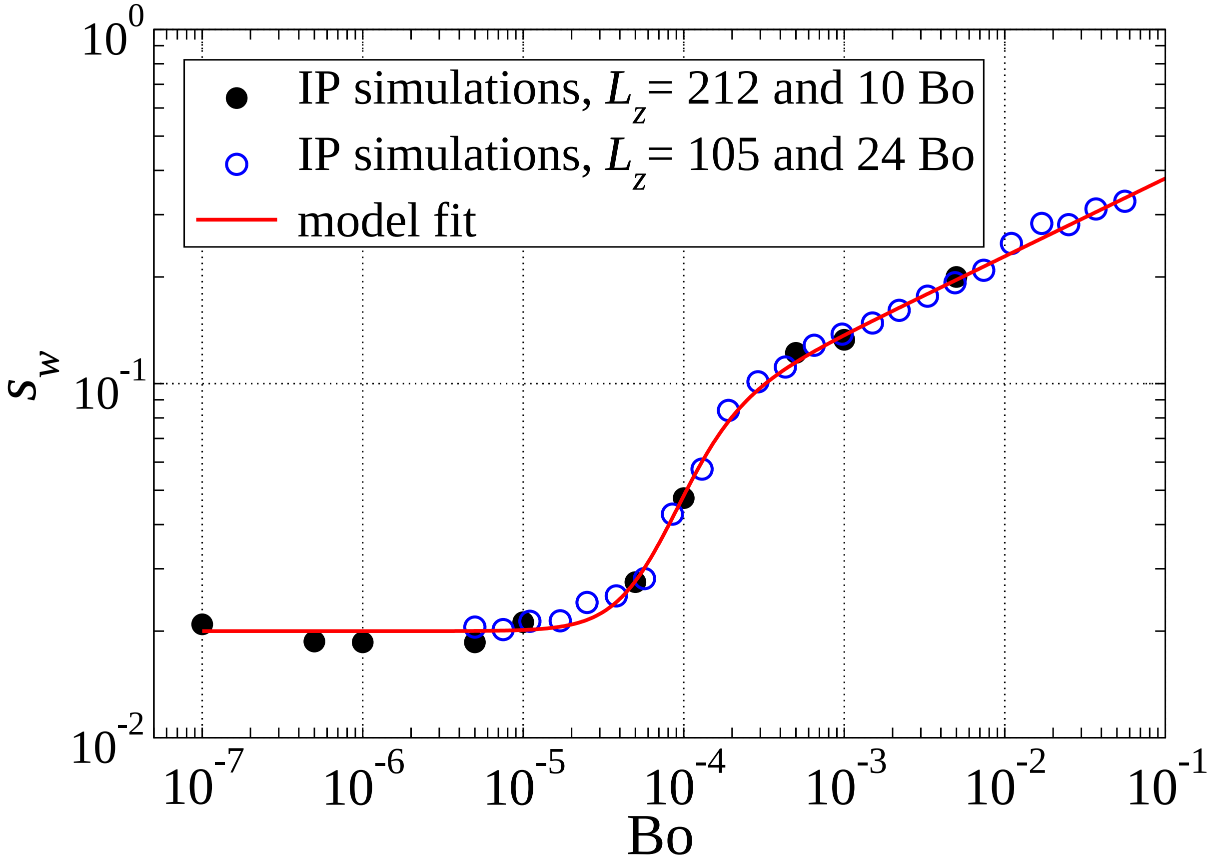

Figure 2.10: Numerical measurements of the invading saturation s_w defined at the point $z = w$ as a function of Bo. The model fit corresponds to Eq. (2.33).

$\mathrm{Bo} \leq \mathrm{Bo_t}$. The model fit given in Figure 2.9 is given by

$$w = w_0 + \frac{\ell_w \mathrm{Bo}^{-\mu} - w_0}{1 + (\mathrm{Bo}/\mathrm{Bo_t})^{-2}}. \tag{2.31}$$

Taking $a_0 = 1$ and $L_x = 18$ for the IP simulations, we have $w_0 = 18^{0.81} = 10.4$ (lattice units). The two free fit parameters that are set to the IP-generated observations of $w(\mathrm{Bo})$ are $\ell_w = 0.7$ (lattice units) and $\mathrm{Bo_t} = 2 \times 10^{-4}$.

For the saturation s_w measured numerically at $z = w$, Figure 2.10 again shows a power law at large Bo transitioning for $\mathrm{Bo} < \mathrm{Bo_t}$ to the constant s_{w0}. The exponent of the power law can be explained by recognizing that across $0 \leq z \leq w$, there are random capillary fingers that have a saturation that scale as in regular IP, $(w/a_0)^{D_c - d}$, such that $s_w = c_{sw} \mathrm{Bo}^{\beta_w}$, where the exponent is

$$\beta_w = \mu(d - D_c) \tag{2.32}$$

or $\beta_w = 0.22$ in 3D. This is precisely the slope seen in Figure 2.10. Allowing for the transition at $\mathrm{Bo_t}$ to constant s_{w0} at low Bond number, the model fit is then given by

$$s_w = s_{w0} + \frac{c_{sw}\mathrm{Bo}^{\beta_w} - s_{w0}}{1 + (\mathrm{Bo}/\mathrm{Bo_t})^{-2}}. \tag{2.33}$$

The two free parameters that are set to the IP simulations of $s_w(\mathrm{Bo})$ are $s_{w0} = 0.02$ and $c_{sw} = 0.63$.

Last, the maximum slope $b_w(\mathrm{Bo})$ of the $s(z)$ curve at the inflection point $z = w$ is given in Figure 2.11. The model fit is given by

$$b_w = b_{w0} + \frac{c_{bw}\mathrm{Bo}^{\omega} - b_{w0}}{1 + (\mathrm{Bo}/\mathrm{Bo_t})^{-2}} \tag{2.34}$$

where the exponent is observed to be $\omega = 0.64$ and $b_{w0} = 2.6 \times 10^{-3}$ (inverse lattice units) and $c_{bw} = 1.06$.

Observables at the residual-saturation transition: ξ, h and s_h

For the maximum size ξ of residual water clusters above $z = h$, we use an identical correlation length argument as was used for w and used by Méheust et al. (2002) and others. However, this time we are focusing on the occupation probabilities $p = 1 - q$ of the water phase and considering the correlation length of the water clusters near percolation of the water phase p_c that takes place in the region $z \geq h$, corresponding to the residual water saturation S_{wc} with capillary pressure $P_c(h)$. We find the following expression,

$$\xi = \ell_\xi \left(\frac{a_0^2}{\gamma} \frac{1}{\xi} \int_{h-\xi}^{h} \frac{\partial P_c(z')}{\partial z'}\, dz' \right)^{-\mu} \tag{2.35}$$

where the length ℓ_ξ is adjusted to fit data. When capillary pressure gradients are variable behind the front due to finite viscous flow, ξ and w are distinct lengths because they involve distinct capillary pressure drops with $w \leq \xi$.

For the case of gravity acting alone at small rates of extraction, $\partial P_c(z)/\partial z = \Delta\rho g$ is a constant (note that gravity is directed in the opposite direction to increasing z) such that

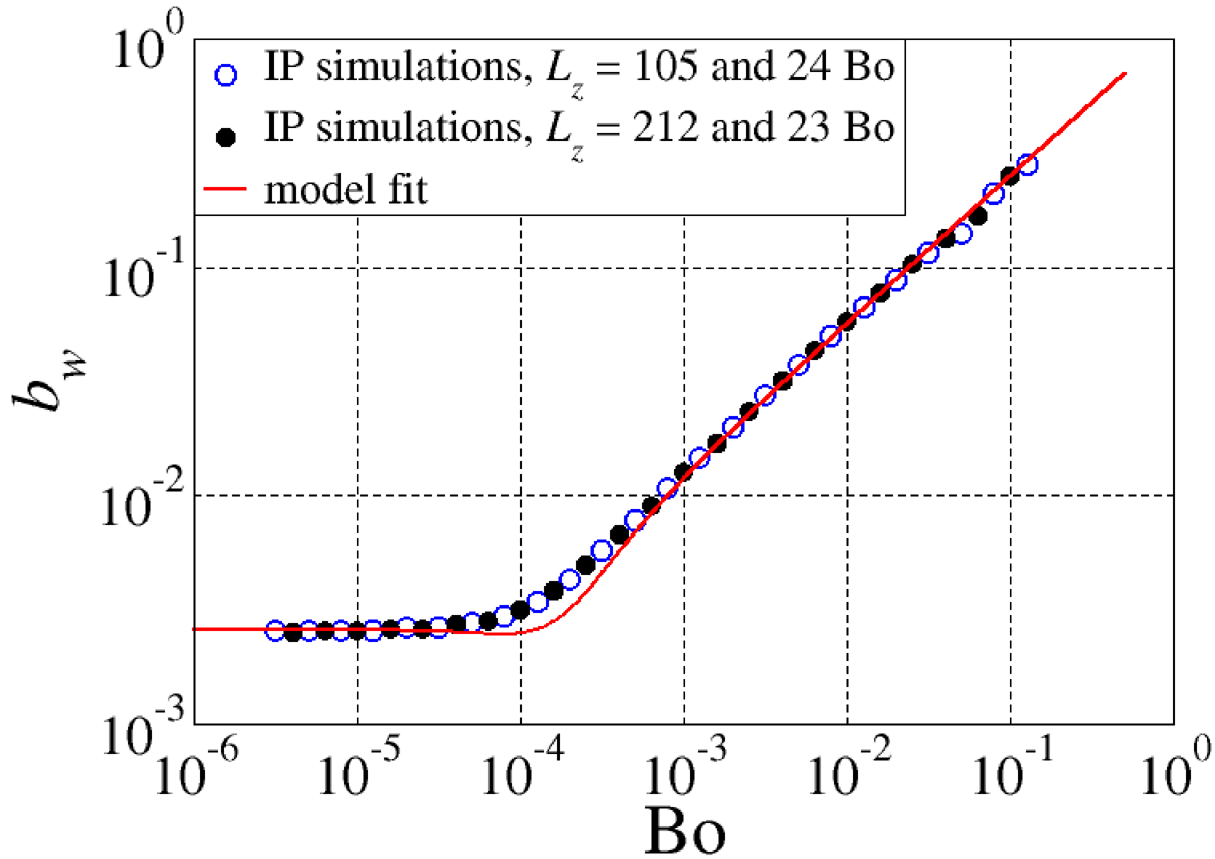

Figure 2.11: Numerical measurements of the slope $b_w = ds(z)/dz|_{z=w}$ of the saturation profile at the point $z = w$. The model fit corresponds to Eq. (2.34).

$w = \xi$. Using the definition of Bo then yields

$$\xi = w = \ell_\xi \mathrm{Bo}^{-\mu} \tag{2.36}$$

which Birovljev et al. (1991) found to fit their 2D measurements on flow through a layer of beads in a Hele-Shaw cell with $\mu = 0.57$, as predicted in 2D.

Wilkinson (1984) defines the transition length h by considering the capillary pressure drop across the distance h to obtain $\gamma/a_h - \gamma/a_0 = \Delta\rho g h$, where $a_h < a_0$ is the smaller pore size being invaded by air at $z = h$. At $z = h$, the capillary pressure is larger compared to at

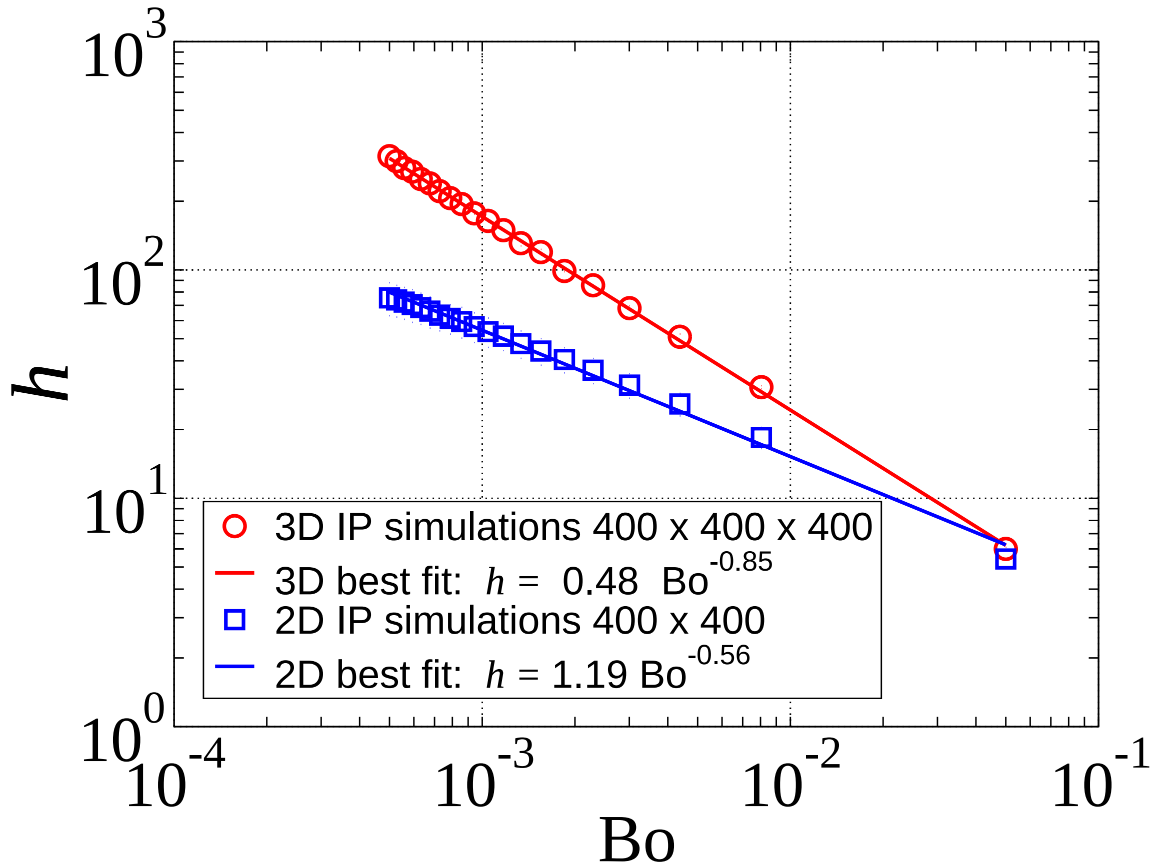

Figure 2.12: Numerical measurements in 2D and 3D of the dual-percolation length h (measured in lattice units) using the fast IP algorithm of Masson (2016) with periodic boundary conditions in the directions lateral to average flow.

$z = 0$ by an amount $\Delta\rho g h$. This can be stated

$$\frac{h}{a_0} = \frac{a_0/a_h - 1}{\mathrm{Bo}}. \tag{2.37}$$

To test the Wilkinson (1984) prediction of $h \propto \mathrm{Bo}^{-1}$, we use the fast algorithm of Masson (2016) and perform numerical IP experiments in a uniform gravity field when trapped clusters of defending fluid are not allowed to be invaded. For simulations conducted on a $400 \times 400 \times 400$ cubic lattice in 3D (and a 400×400 square lattice in 2D) with periodic boundary conditions in the directions lateral to average flow, we observe a different scaling for h, as shown in Figure 2.12, with $h \propto \mathrm{Bo}^{-0.85}$ (exponent $\neq$ -1).

Given these IP simulations, we propose that the length h will satisfy a scaling of similar form to w and ξ, but with a different exponent μ_h; i.e., h should depend on the difference in the capillary pressure across the dual percolation region so that

$$h = \ell_h \left(\frac{a_0^2}{\gamma} \frac{1}{h} \int_0^h \frac{\partial P_c(z')}{\partial z'} \, dz' \right)^{-\mu_h} \tag{2.38}$$

where ℓ_h is a pressure-independent length that must be adjusted to fit data. For the case of gravity alone, we then have

$$h = \ell_h \mathrm{Bo}^{-\mu_\mathrm{h}} \tag{2.39}$$

As shown in Figure 2.12, we numerically measure h in both 2D and 3D and observe the scalings

$$h = \begin{cases} 0.48\mathrm{Bo}^{-0.85} & \text{in 3D} \\ 1.19\mathrm{Bo}^{-0.56} \approx \xi & \text{in 2D} \end{cases} \tag{2.40}$$

In 2D, we observe numerically that $h \approx \xi$. Once the size of the "fjords" of defending fluid, which extend from the front region into the invaded region, become comparable to the correlation length ξ, they are pinched off. This results in the defending fluid becoming completely disconnected at distances ξ or greater behind the front, with the result that $w = \xi \approx h$.

In 3D, the additional spatial degree of freedom for the defending fluid allows the fjords to remain continuous into the invaded region even when the entrance to a fjord becomes pinched off in places. Only at a distance $h > \xi$ will a fjord finally become completely closed off in all three space dimensions, and that distance h will increase with the decreasing influence of gravity. In the absence of gravity in 3D, the fjords are never entirely cut off, $h \to \infty$, and the residual saturation of the defending fluid is close to zero, while the saturation of the invading nonwetting fluid is S_{nc}^{∞} as given earlier for Bo = 0. Determining the exponent μ_h in the scaling $h = \ell_h \mathrm{Bo}^{-\mu_\mathrm{h}}$ in terms of standard percolation critical exponents is not obvious and we settle for observing its value from the numerical IP experiments of Figure 2.13.

We could equivalently restate the above using the Wilkinson (1984) result of Eq. (2.37) by saying that a_h (the size of pores being invaded at $z = h$ where defending fjords are being entirely pinched off in all directions) is a function of Bond number and given by

$$a_h(\mathrm{Bo}) = \frac{\mathrm{a}_0}{1 + \mathrm{Bo}^{1-\mu_\mathrm{h}}}, \tag{2.41}$$

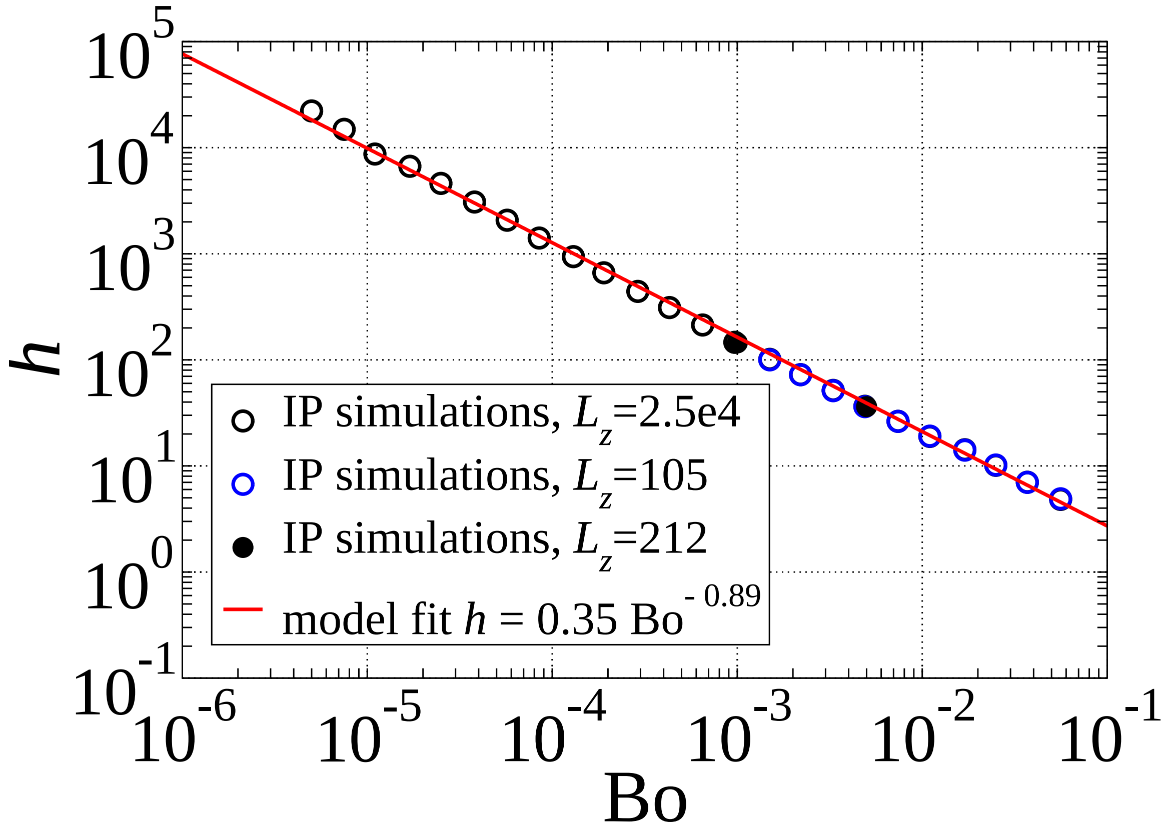

Figure 2.13: Numerical measurements of the dual-percolation length h measured in lattice units using the fast IP algorithm of Masson (2016) on systems of size $18 \times 105 \times L_z$ with no flow boundary conditions in the directions lateral to average flow and $L_z = 105, 212$ and 2.5×10^{-4} (lattice units) in the direction of flow.

which behaves properly at $\mathrm{Bo} = 0$ and results in Eqs. (2.37) and (2.39) being identical.

For an IP system of lateral dimensions 18×105 (the dimensions of our laboratory flow cell), flow-length dimensions of 105, 212 and 2.5×10^4, and no-flow boundary conditions in the lateral directions, we observe in Figure 2.13 a slightly different scaling of $h \propto \mathrm{Bo}^{-0.89}$. The no-flow versus periodic lateral boundary conditions may have a slight influence on the exponent. In connecting to lab data, we will use the $h \propto \mathrm{Bo}^{-0.89}$ scaling.

The saturation $s_h = s(h)$ at the point $z = h$ where the residual saturation region begins has been estimated by Wilkinson (1984) in his appendix to scale as

$$s_h = s_{h0} + \tilde{c}_{sh}\left(\frac{\xi}{a_0}\right)^{-(1+\beta)/\nu} \tag{2.42}$$

$$= s_{h0} + c_{sh}\mathrm{Bo}^{(1+\beta)/(1+\nu)} \tag{2.43}$$

where the exponent β is a standard exponent of ordinary percolation that controls how the fraction of defending water sites belonging to the infinite cluster of water in regular percolation increases above the percolation threshold s_{h0}. In 3D, $\beta = 0.418$, $\nu = 0.875$ (the correlation-length exponent), while for a cubic IP lattice, $s_{h0} = 0.66$ (Wilkinson, 1984). Note that the only place in the description of the drainage fronts being developed here where ξ is used is in the determination of the nonwetting saturation s_h of the residual saturation region, and we elect to work with Eq. (2.43) written as $s_h = s_{h0} + c_{sh}\mathrm{Bo}^{\beta_\mathrm{h}}$ where

$$\beta_h = \frac{1+\beta}{1+\nu} \tag{2.44}$$

or $\beta_h = 0.756$ (3D).

Functional form of $s(z)$

In 3D, the local nonwetting fluid saturation profile $s(z)$ observed in IP simulations is constrained by the five observables w, $s_w = s(w)$, $b_w = ds/dz|_{z=w}$, h and $s_h = s(h)$. All of these scale with Bo according to the rules given in the previous subsections. At the point $z = 0$, we expect the slope to be zero and the local curvature to be positive with a monotonically increasing slope until the slope b_w is attained at the inflection point $z = w$. Between $z = w$ and $z = h$, the slope will monotonically decrease until it is zero at $z = h$.

We thus separate the $s(z)$ model into three regions behind the front

$$s(z) = \begin{cases} s_a(z) & \text{for } 0 < z < w \\ s_b(z) & \text{for } w \le z \le h \\ s_h & \text{for } z > h. \end{cases} \tag{2.45}$$

A simple power law increase for $s_a(z)$ with increasing z does an excellent job matching the numerical (IP) and laboratory observations of the saturation profile,

$$s_a(z) = s_w\left(\frac{z}{w}\right)^{b_w w/s_w}. \tag{2.46}$$

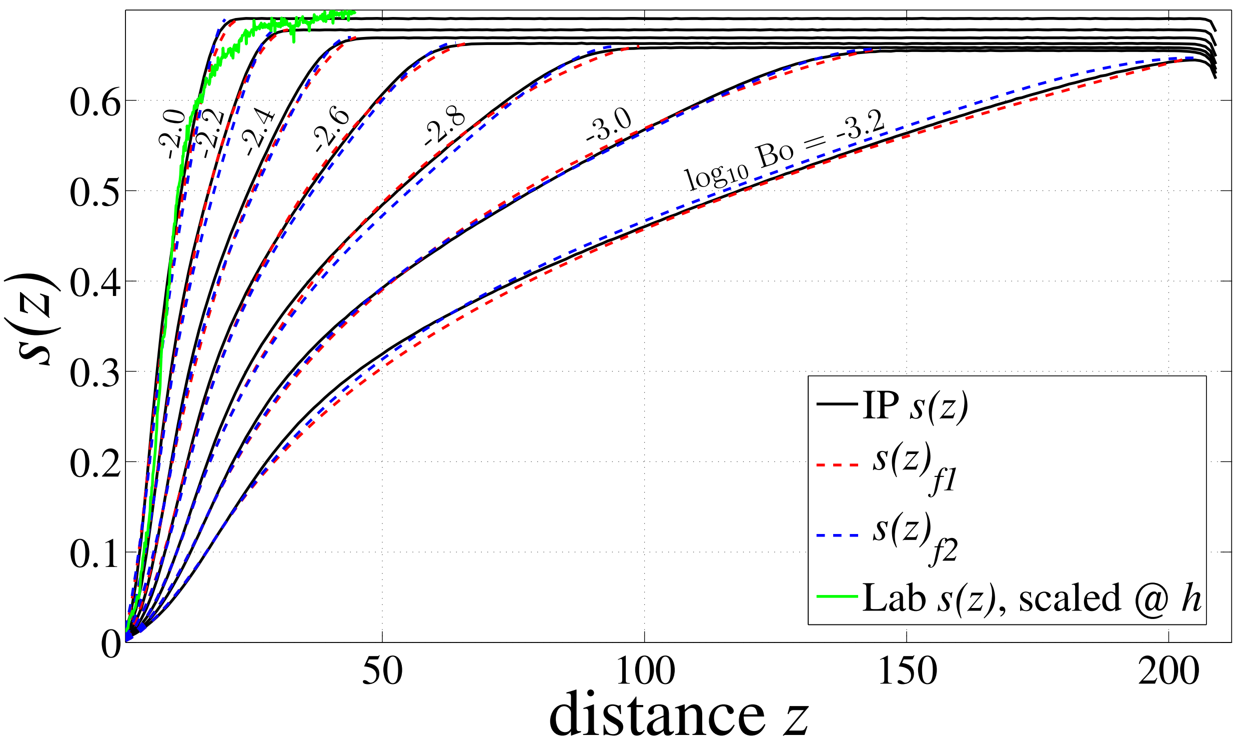

Figure 2.14: Saturation profiles ($s(z)$) from IP simulations (black) at variable Bo are plotted alongside the functions given by equation 2.45 with Eqs. 2.48 (red) and 2.50 (blue). From left to right, $log_{10}(\text{Bo}) = [-2.0, -2.2, -2.4, -2.6, -2.8, -3.0, -3.2]$. A laboratory observation of $s(z)$ at $log_{10}(\text{Bo}) = -2.1$ (air/water) is shown in green. It is scaled at h to match the predictions of Eqs. 2.43 and 2.40

.

To find an appropriate functional form for $s_b(z)$, we first write

$$s_b(z) = s_h - (s_h - s_w)f(z) \tag{2.47}$$

and look for a function $f(z)$ that has a slope $df(z)/dz|_{z=w} = -b_w/(s_h - s_w)$ at $z = w$ and then monotonically transitions to zero slope at $z = h$. This function also must satisfy $f(w) = 1$ and $f(h) = 0$. There are an infinity of functions $f(z)$ that can satisfy these constraints. A challenge is that the shape of the saturation curve between $z = w$ and $z = h$ changes with decreasing Bo. We will give two functions for $f(z)$ that do a reasonable job of matching the numerical and laboratory data.

A first possible functional form is

$$f_1(z) = \left(\frac{h-z}{h-w}\right)^{\frac{b_w(h-w)}{(s_h-s_w)}-\alpha_f} \left[1 + \frac{\alpha_f}{\beta_f}\left(\frac{z-w}{h-w}\right)\right]^{-\beta_f}. \tag{2.48}$$

Formally, the exponents α_f and β_f can take any value and the constraints on $f(z)$ will be satisfied. We find that a good fit is obtained by taking $\beta_f = 1/3$ for all Bo and taking α_f to be a simple linear function of the dimensionless ratio w/h, which is a function of Bo as given above

$$\alpha_f = \alpha_{f0}\left(1 - \alpha_{f1}\frac{w}{h}\right). \tag{2.49}$$

A good fit to the observations is obtained with $\alpha_{f0} = 3.7$ and $\alpha_{f1} = 15.9$. Other, more complicated, nonlinear functions for $\alpha_f(w/h)$ may provide a better fit.

An alternative form with fitting exponents that are independent of Bo is

$$f_2(z) = \frac{(1-c_f)^{\delta_f}}{[1-(w/h)^{\beta_f}]^{\tau_f}} \frac{\left[1-(z/h)^{\beta_f}\right]^{\tau_f}}{[1-c_f(z/w)^{-\alpha_f}]^{\delta_f}} \tag{2.50}$$

where the constant c_f is defined in terms of another constant γ_f as

$$c_f = \frac{\gamma_f}{1+\gamma_f} \tag{2.51}$$

with

$$\gamma_f = \frac{1}{\delta_f \alpha_f}\left[\frac{w\, b_w}{s_h - s_w} - \tau_f \beta_f \frac{(w/h)^{\beta_f}}{1-(w/h)^{\beta_f}}\right]. \tag{2.52}$$

It is strictly required that $\tau_f > 1$ in order for the slope to be zero at $z = h$. The other exponents α_f, β_f and δ_f have no constraints. After exploring a range of possibilities, we find that taking $\alpha_f = 0.8$, $\beta_f = \delta_f = 5$ and $\tau_f = 2$ does an adequate job of fitting the IP data as a function of Bo. The fits to the IP data using the above $f_1(z)$ and $f_2(z)$ are shown in Figure 2.14.

In either of these two functions $f_1(z)$ and $f_2(z)$, all Bo dependence of the shape of the curves is controlled by the Bo dependence of w and h as given earlier. There certainly exist other functions for $f(z)$ that can fit the data better, but they will have a more complicated form. We will use $f_2(z)$ going forward due to its relative simplicity. We implicitly assume that the $f_2(z)$ exponents $\alpha_f = 0.8$, $\beta_f = \delta_f = 5$ and $\tau_f = 2$ are universal and applicable to any material.

When applying the above model for $s(z)$ to different porous media, the parameters expected to change from material to material are ℓ_h, ℓ_w, c_{sh}, c_{bw}, c_{sw}, s_{h0}, b_{w0}, and w_0, which all depend on the details of the network of pores involved. Conversely, the exponents $\mu = 0.467$, $\mu_h = 0.845$, $\omega = 0.64$, $\beta_w = 0.87$, and $\beta_h = 1.62$ are assumed to have universal values that apply to any 3D porous material. In Figure 2.14, we plot $s(z)$ over a range of Bo values in the vicinity of our experiment (Bo $= 7.4 \times 10^{-3}$). The IP results in black are captured well by the models of $s(z)$ in red and blue. The hydrostatic curve observed in our experiment is re-plotted from Figure 2.3 in green, and scaled to match the values of h and s_h predicted by Eqs. 2.43 and 2.40. The values of h agree if the lattice spacing is equal to four times our mean grain diameter, which suggests that the percolation node spacing represents the average distance traversed by a meniscus during a Haines jump, rather than the distance between adjacent pores. As shown in Figure 2.3, residual water saturation in the experiment is much lower than expected from the IP simulations, which may indicate that thin film flows are an important drainage mechanism at lower water saturation (e.g., Nimmo, 2010).

Saturation Models when $\mathrm{Bo} > 0$ and $\mathrm{Ca} > 0$

Finally, we address the more challenging problem of the capillary number dependence in $s(z)$. When the defending liquid in stable drainage is being extracted from a voxel at a rate where the viscous pressure drop is no longer negligible compared to the capillary pressure drop across a meniscus, Wilkinson (1984) and later Méheust et al. (2002) note that the gravitational pressure drop is partially undone by the viscous pressure drop.

The viscous pressure gradient is determined from Darcy's law as

$$\frac{\partial P_v}{\partial z} = -\frac{q_w \eta_w}{k_o \kappa_w(S_w)}. \tag{2.53}$$

One challenge is that it will not be uniform throughout the region $0 \leq z \leq h$ due to varying saturation, but it must, in general, be numerically determined as part of the dynamic modeling of Eqs. (2.1) and (2.2).

However, in applying to the 1D experimental observations of $s(z)$, we can estimate the viscous pressure gradient analytically in the following approximate manner. Assume that the saturation profile $s(z)$ is simply advancing through the flow cell with the average flow speed v_z, controlled by the rate of water extraction from the bottom of the cell. This is consistent with our observations and will generally be the case when the hydraulic conductivity is much larger than the Darcy velocity (Hoogland et al., 2015). If we denote the position of the advancing lead menisci at any instant as $z_o(t)$, the approximation is that the saturation profile evolves through time as $s(z,t) = s(z - z_o(t))$, where the function $s(z)$ is again determined from the IP result of Eq. (2.45), but with w, ξ and h now satisfying new Ca-dependent scalings. The constant speed that the profile advances with is given by

$$v_z = \frac{dz_o(t)}{dt} = -\frac{1}{\phi}\frac{k_o}{\eta_w}\left.\frac{\partial P_v}{\partial z}\right|_{z\le z_o(t)} \tag{2.54}$$

where the viscous pressure gradient is assumed to be uniform ahead of the front ($z < z_o(t)$).

The rate at which the water saturation $S_w(z,t)$ is changing can then be approximated as

$$\begin{aligned}\phi\frac{\partial S_w(z-z_o(t))}{\partial t} &= -\phi\frac{\partial S_w(z-z_o(t))}{\partial z}\frac{dz_o(t)}{dt} \\ &= \frac{k_o}{\eta_w}\left.\frac{\partial P_v}{\partial z}\right|_{z\le z_o(t)}\frac{\partial S_w}{\partial z}.\end{aligned} \tag{2.55}$$

From Eq. (2.1) for the conservation of water mass in 1D, we also have

$$\begin{aligned}\phi\frac{\partial S_w(z,t)}{\partial t} &= -\frac{\partial q_w(z,t)}{\partial z} \\ &= \frac{k_o}{\eta_w}\frac{\partial}{\partial z}\left[\kappa_w(S_w)\frac{\partial P_v(z,t)}{\partial z}\right]\end{aligned} \tag{2.56}$$

which upon equating Eqs. (2.55) and (2.56) gives

$$\left.\frac{\partial P_v}{\partial z}\right|_{z\le z_o(t)}\frac{\partial S_w(z,t)}{\partial z} = \frac{\partial}{\partial z}\left[\kappa_w(S_w)\frac{\partial P_v(z,t)}{\partial z}\right]. \tag{2.57}$$

In order to determine how the viscous pressure gradient is varying with z, we consider the moment in time when $z_o(t) = 0$ and integrate from a point z in the profile to h to obtain

$$\begin{aligned}&\left.\frac{\partial P_v}{\partial z}\right|_{z\le 0}[S_w(h) - S_w(z)] = \\ &\qquad \kappa_w(S_w(h))\left.\frac{\partial P_v(z)}{\partial z}\right|_{z=h} - \kappa_w(S_w(z))\frac{\partial P_v(z)}{\partial z}.\end{aligned} \tag{2.58}$$

Now at $z = h$, the relative permeability of the water goes to zero ($\kappa_w(S_w(h)) = 0$) while $S_w(h) = S_{wc} = 1 - s_h$ is the residual water saturation in the region $z \ge h$. We then obtain the result for the viscous pressure gradient as

$$\frac{\partial P_v(z)}{\partial z} = \left[\frac{S_w(z) - S_{wc}}{\kappa_w(S_w(z))}\right] \left.\frac{\partial P_v}{\partial z}\right|_{z\leq 0}. \tag{2.59}$$

The boundary condition at $z = h$ is that the water's Darcy velocity goes to zero. This is the requirement that $\kappa_w(S_w(z))\partial P_v(z)/\partial z \to 0$ as $z \to h$, which is satisfied by Eq. (2.59). At $z = 0$, we would like $\partial P_v(z)/\partial z|_{z=0} = \partial P_v/\partial z|_{z\leq 0}$. This can be achieved either by selecting $S_w(0)$ to have a particular value less than one, or by assuming $S_w(0) = 1$ and requiring the relative permeability to have the value $\kappa_w(S_w(0)) = 1 - S_{wc}$ at $z = 0$. Either approach gives the same final result in the analysis that follows, but we choose the second option.

To address how the scalings of w, ξ and h depend on the viscous pressure gradient, we note that flow and saturation distribution behind the front are controlled by the gradient in the capillary pressure $\partial P_c/\partial z = \partial P_n/\partial z - \partial P_w/\partial z \approx -\partial P_w/\partial z$, which in the presence of both gravity and finite viscous flow is

$$\frac{\partial P_c(z)}{\partial z} = \Delta\rho g - \left[\frac{S_w(z) - S_{wc}}{\kappa_w(S_w(z))}\right] \left.\frac{\partial P_v}{\partial z}\right|_{z\leq 0}. \tag{2.60}$$

Defining the capillary number Ca as that in the pure liquid ahead of the front

$$\mathrm{Ca} = \frac{a_0^2}{\gamma} \left.\frac{\partial P_v}{\partial z}\right|_{z\leq 0} \tag{2.61}$$

the earlier scaling rules of Eqs.(2.28), (2.36) and (2.38) for w, ξ and h now become

$$w = \ell_w \left[\mathrm{Bo} - \mathrm{A_w Ca}\right]^{-\mu} \tag{2.62}$$

$$\xi = \ell_\xi \left[\mathrm{Bo} - \mathrm{A}_\xi \mathrm{Ca}\right]^{-\mu} \tag{2.63}$$

$$h = \ell_h \left[\mathrm{Bo} - \mathrm{A_h Ca}\right]^{-\mu_h} \tag{2.64}$$

where the dimensionless capillary-number "amplification factors" are defined as

$$A_w = \frac{1}{w}\int_0^w \frac{S_w(z) - S_{wc}}{\kappa_w(S_w(z))}\, dz \tag{2.65}$$

$$A_\xi = \frac{1}{\xi}\int_{h-\xi}^h \frac{S_w(z) - S_{wc}}{\kappa_w(S_w(z))}\, dz \tag{2.66}$$

$$A_{hw} = \frac{1}{h-w}\int_w^h \frac{S_w(z) - S_{wc}}{\kappa_w(S_w(z))}\, dz. \tag{2.67}$$

$$A_h = \frac{w}{h}A_w + \left(1 - \frac{w}{h}\right) A_{hw}. \tag{2.68}$$

Inserting Eqs. (2.65)–(2.68) into Eqs. (2.62)–(2.64) provides a set of three coupled nonlinear equations that must be solved iteratively to find the roots w, ξ and h that are functions of Bo and Ca.

To proceed, we need a particular model for the water's relative permeability. Although the earlier models of van Genuchten and Corey for the water- and gas-phase relative permeability can certainly be employed, it is more consistent to take a percolation perspective (e.g., Kirkpatrick, 1973; DeGennes, 1983) and write the relative permeability function for water in the percolation form

$$\kappa_w(z) = \frac{(S_w(z) - S_{wc})^{t_w}}{(1 - S_{wc})^{t_w - 1}} \quad \text{for} \quad S_{wc} < S_w \leq 1 \tag{2.69}$$

and $\kappa_w = 0$ when $S_w \leq S_{wc}$. A similar form can be assumed for the gas phase. This particular expression gives $\kappa(S_w(0)) = 1 - S_{wc}$ if we take $S_w(0) = 1$, which insures that Eq. (2.59) reduces to the correct expression at $z = 0$. The conductivity exponent t_w has a universal 3D value that has been reported in the range $3/2 < t_w < 2$, but is generally considered to be close to 2. The residual water saturation has the predicted value of $S_{wc} = 1 - s_h$, where s_h was given earlier by the scaling of Eq. (2.43).

In order to use the function $s(z)$ of Eq. (2.45) in the determination of the amplification factors, we write $S_w(z) = 1 - s(z)$ to give the integrand of each amplification factor as

$$\frac{S_w(z) - S_{wc}}{\kappa_w(S_w(z))} = \frac{s_h^{t_w - 1}}{[s_h - s(z)]^{t_w - 1}} \tag{2.70}$$

which shows that t_w must be less than 2 in order for the amplification factors A_ξ and A_h to remain integrable at $z = h$. The closer that t_w is to 2, the larger the amplification factors will become.

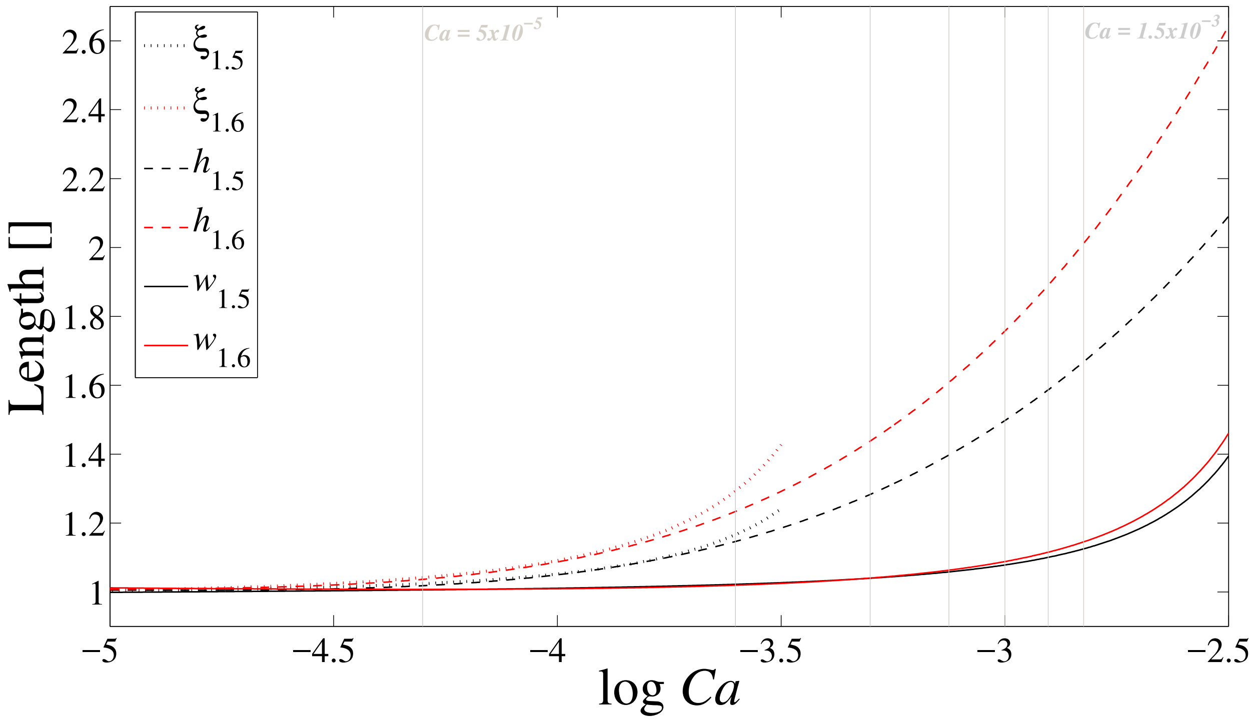

Figure 2.15: The lengths w, h, and ξ are plotted as a function of Ca relative to their low Ca limit at two values of the conductivity exponent: $t_w = 1.5$ and $t_w = 1.6$. Grey vertical lines indicate the Ca values of our laboratory experiments.

One approach for obtaining the lengths w, ξ and h is to use successive approximations. Beginning with a first guess for A_w, A_ξ and A_{hw}, use Eqs. (2.62)–(2.64) to make a first estimate of w, ξ and h, and then use these first estimates in Eqs. (2.65)–(2.68) to update the amplification factors, repeating in this manner until the lengths do not change.

Comparison to Laboratory Observations

We now compare the above saturation-profile model with the saturation profiles measured optically in our flow cell. To do so, we first determine how the amplification factors and lengths vary with Ca for parameters corresponding to the laboratory experiments. As such, we take Bo $= 7.4 \times 10^{-3}$, and we set the other free parameters of the model according to the Ca $= 0$ values of section 3.2. Figure 2.15 shows the results of this calculation with permeability exponent $t_w = 1.5$ and $t_w = 1.6$. Each length is normalized by its low Ca limit. We find the expected result that increasing t_w (though not exceeding 2) increases lengths at any given Ca and causes the lengths to diverge at smaller Ca. We also find that h is more sensitive to Ca than w, and that ξ diverges at relatively small Ca.

In Figure 2.16, we use the Ca dependence of w and h to predict the water saturation

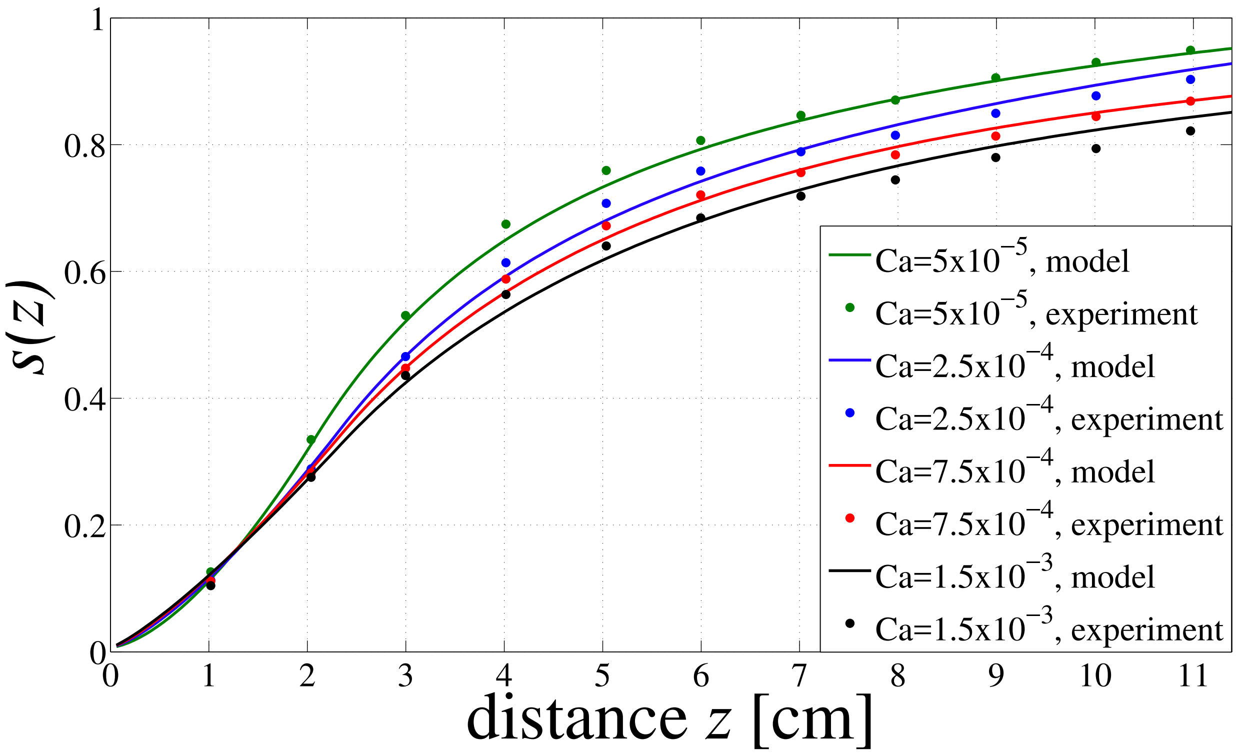

Figure 2.16: The model of equation 2.45 is plotted at four Ca values, with Ca-dependent lengths given by Eqs. 2.62-2.64 (and as plotted in Figure 2.15). The value of the conductivity exponent is $t_w = 1.5$. Corresponding observations from laboratory drainage experiments are scattered at 1 cm intervals.

profiles observed in our flow cell, which are scatter plotted at 1 cm intervals. These observations were obtained by performing a moving average of $s(z)$ across all video frames for the duration of the flows, each at a unique Ca. For clarity, we show a subset of the experiments (Ca $=$ 5x10^{-5}, Ca $=$ 2.5x10^{-4}, Ca $=$ 7.5x10^{-4}, Ca $=$ 1.5x10^{-3}). We fit our $s(z)$ model from equation 2.45 to the lowest Ca experiment (Ca $= 5.0 \times 10^{-5}$) and, keeping s_h fixed, adjust w and h according to the results of Figure 2.15 with $t_w = 1.5$.

2.5 Conclusion

Stable drainage experiments have been performed (air invading water-saturated glass beads in a 3D flow cell) while optically measuring the 2D spatial distribution of saturation (the optical transmission measurements averaged over the width of the cell). The measurements show that the saturation profile $s(z)$ is dependent on the capillary number Ca, with larger Ca producing more extended saturation profiles. Invasion percolation simulations demonstrate the effect of variable Bo on $s(z)$. In order to explain these observations, a percolation-based model was developed. A scaling form for the saturation versus distance relation was proposed with profile shape exponents determined from Invasion Percolation numerical experiments. This form has explicit dependence on two key lengths: w, the width of the invasion front, defined here as the inflection point where the saturation profile goes from positive to negative curvature, and h, the width of the entire region behind the front where both fluid phases percolate. A third length ξ, defined as the maximum size of trapped water clusters in the residual saturation region $z > h$, more weakly influences the residual water saturation. All three lengths w, h and ξ are shown to have both Bo and Ca dependence. The critical nonwetting saturation S_{nc} at which a voxel at the front is first percolated was optically measured and shown to have dependence on the size of the voxel L_z, as well as on Bo and Ca. The main contribution of this work is a model for $s(z)$ which can be used to determine $S_{nc}(\mathrm{Bo}, \mathrm{Ca}, \mathrm{L_z})$. It applies to stable drainage scenarios and will be useful for macroscopic porous-continuum modeling of two-phase flow.

Chapter 3

Shaking water out of sands: an experimental study

This chapter is adapted with minor changes from: Breen, S. J., Zhang, Z., and Wang, C.-y. (2020), Shaking water out of sands: an experimental study, Water Resources Research, 56.

3.1 Summary

Strong earthquakes can cause different kinds of hydrological responses, and several mechanisms have been suggested to explain them. Verification of these mechanisms, however, is often lacking. Here we test some hypotheses with a laboratory experiment, in particular the hypothesis that dynamic strain mobilizes trapped water in the unsaturated zone. We construct a sand chamber, partially saturated with water, and subject it to "seismic" shaking of controlled energy. Pore pressure in the saturated and unsaturated zones is monitored before and after shaking. We identify three distinct mechanisms: consolidation of sediments in the saturated zone, release of capillary water from the capillary fringe, and mobilization of isolated pore water in the unsaturated zone. Each mechanism may cause pore pressure in the saturated zone to suddenly increase with shaking, and each may offer new insights to understand the source of the extra water and other shallow hydrological responses that appear after earthquakes.

3.2 Introduction

Different kinds of hydrological responses to earthquakes have been reported, including increased streamflow (e.g., Rojstaczer and Wolf, 1992; Muir-Wood and King, 1993), changes of groundwater level (e.g., Blanchard and Byerly, 1935), changes of water composition (e.g., Claesson et al., 2004; Tokunaga, 1999), and liquefaction (e.g., Schmidt, 1875). However, the mechanisms for many such responses have not been verified (e.g., Wang et al., 2017). One example is the debate over the source of extra water that appears in coseismic increases of streamflow and groundwater level. In some cases, unequivocal evidence that the new water comes from nearby mountains is provided by its isotopic compositions of oxygen and hydrogen (e.g., Claesson et al., 2004; Claesson et al., 2007; Wang et al., 2004; Wang and Manga, 2015). In most other cases, however, no such evidence is available, and other explanations are required. For instance, coseismic increases in streamflow (Manga et al., 2016) and water level (Wang et al., 2017) following some induced earthquakes in Oklahoma occurred far from any elevated topography. Also, the recent Puerto Rico earthquake swarm of 2019-2020 caused well-level and streamflow responses in the vicinity of Guayanilla. As shown in Figure 3.1a, the water level in the closest well to the swarm epicenters, situated in an unconfined, alluvial aquifer, increased in response to the largest earthquake of the swarm on Jan. 7 (M_w6.4, 10 km S of the well, 10 km depth), and again on Jan. 10 in response to a nearby, shallow event (M_w4.8, 2 km S of the well, 4 km depth). After these earthquakes, the water level remained elevated. In addition, the discharge along Rio Guayanilla, measured a few km N of the well, increased concurrently by a sustained 3-4 cfs after the Jan. 7 earthquake (Figure 3.1b). While these events are consistent with previous works on coseismic hydrological responses (e.g. Wang and Manga, 2010), there is no apparent source to explain the extra water.

Following the 2010 M_w8.8 Maule (Chile) earthquake, Mohr et al. (2015) proposed a new mechanism to explain increased streamflow in a headwater catchment in the Chilean coastal range. According to this mechanism, the additional water is released from the unsaturated zone when the seismic energy density is sufficient to overcome the threshold of soil water retention. While interesting, this mechanism has not been experimentally or quantitatively verified, and it is difficult to differentiate it from the competing hypothesis that the excess water may come from coseismic consolidation of saturated soils (e.g., Wang et al., 2001).

In this work, we construct a sand chamber and subject it to seismic shaking of controlled energy while progressively lowering the water table from above the sand surface to below. Pore pressure in the saturated and unsaturated zones is monitored before and after shaking. We show that pore pressure in the saturated zone suddenly increases with shaking in response to compaction when the water level is above the surface and in response to disturbance of capillary forces when the water table is below the surface. We also show that: (1) pore pressure remains elevated indefinitely when an unsaturated zone is present; (2) that water transports downward from the residual saturation region; and (3) that pore pressure responds faster to disturbance of capillary forces than to coseismic consolidation, providing a quantitative criterion to differentiate the two processes. These new mechanisms offer new insight to understand the source of the extra water and other shallow hydrological responses that appear after earthquakes.

3.3 Experimental Setup

To study the effect of seismic shaking on hydrological processes, we constructed a 1.5m tall, rectangular sand column using clear acrylic panels, with dimensions 20 cm x 20 cm in cross-section (Figure 3.2). The experiment took place in a basement laboratory with cool

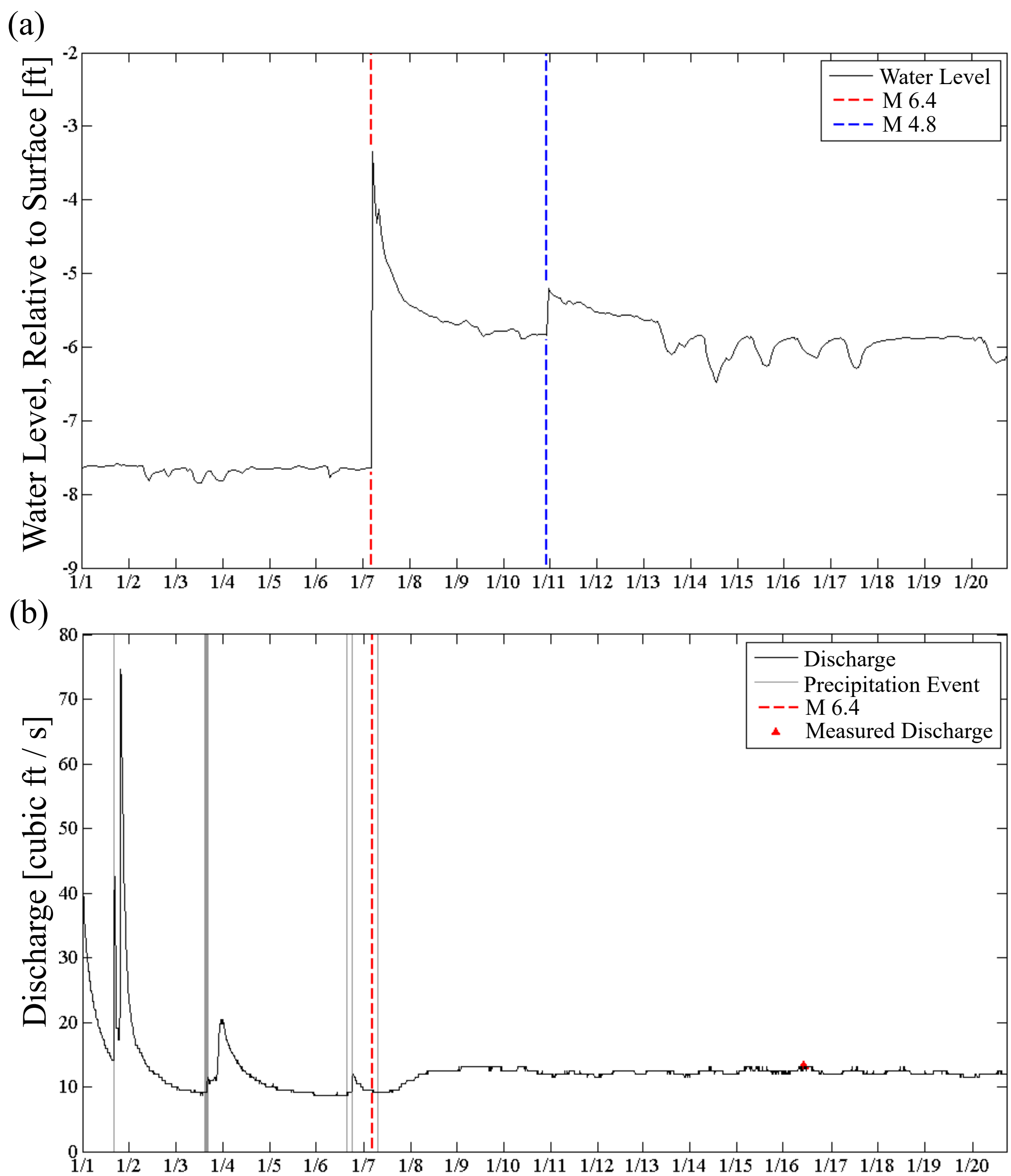

Figure 3.1: (a) The water level at a well in Guayanilla, Puerto Rico increased in response to earthquakes on Jan. 7 and Jan. 10 (USGS site number 180052066471000). (b) Discharge at nearby Rio Guayanilla increased by 3-4 cfs following the Jan. 7 earthquake (USGS site number 50124200). This increase was more gradual than the increases caused by precipitation events.

and stable air conditions. The column rests on a structurally reinforced water reservoir with dimensions 10 cm x 35 cm x 35 cm and is hydraulically connected to it through a perforated plate overlain by a fine wire mesh. A thin rubber gasket creates a water-tight seal at the column/reservoir interface. To monitor and adjust the water level in the column, the reservoir is connected to a tall standpipe. The valve between the reservoir and standpipe is open when adjusting the water level in the sand column and closed during impact experiments to prevent flow out of the column and reservoir. We installed a calibrated 0-5 psi pressure sensor (American Sensor Technologies, AST47LP) 10 cm above the bottom of the chamber to measure pore pressure in the saturated zone and water table height. Its output signal is captured continuously by a digital storage oscilloscope at a sampling rate of 10 Hz. We also installed ten flow cell tensiometers (Soil Measurement Systems, C1-029B) at 10 cm intervals from the top of the chamber to measure water tension in the upper, unsaturated region of the sand. Each tensiometer's output signal is passed through an amplifying circuit and, prior to installation, calibrated with a manometer. Tensiometer data was recorded by hand just before shaking and approximately one day after (tensiometers are routinely used to measure diurnal changes in soil moisture). Finally, we also installed an external smartphone accelerometer (Accelerometer Meter) 10 cm above the bottom of the chamber, adjacent to the pressure sensor.

We filled the chamber with Ottawa F-50 sand (median grain size is equivalent to sieve size 50, or 0.3 mm) by pouring continuously from above in order to minimize micro-layering. The hydraulic conductivity of this sand is 0.025 to 0.038 cm/s (Kramer, 2013). Based on bulk density, porosity was $\phi = 0.358 \pm 0.003$ ($\phi = 1 - \rho_{bulk}/\rho_{particle}$, where ρ_{bulk} is the mass of sand added to the chamber divided by its volume, and $\rho_{particle}$ is 2.65 g/cm^3). Ottawa sands are widely studied and characterized because they are relatively uniform in composition with rounded particles, and because they have a steady commercial supply (Bastidas, 2016), but we acknowledge that soil structure and texture may affect the way that pore pressure and groundwater transport respond to earthquakes. The water retention function of our F-50 sand, shown in Figure 3.4, was determined independently by Vaz et al. (2002). To saturate with water, we first flowed CO_2 to displace as much air as possible and then filled slowly with deionized water at a rate of 100 ml/min.

To shake the chamber in a controlled fashion, we impacted the side of the reservoir with a 3.6 kg iron ball on a track, released from a height of 40 cm above the impact pad. This imparts an energy density of O(100) J/m^3 to the sand, which was the key variable in Mohr et al. (2015) and is similar in magnitude to their estimates for the Chilean field site. This energy density corresponds to the near field and is above the threshold for liquefaction ($\sim$10 J/m^3, Wang and Manga, 2010). It is also far above the threshold for groundwater effects. Energy densities larger than 10 J/m^3 should result in undrained consolidation and abrupt water level increases, which we observed in our experiments. We recognize that an impact is not a perfect analog of seismic shaking, however, and the accelerations from the impact are of shorter duration, larger peak amplitude, and higher frequency than would occur during a large earthquake.

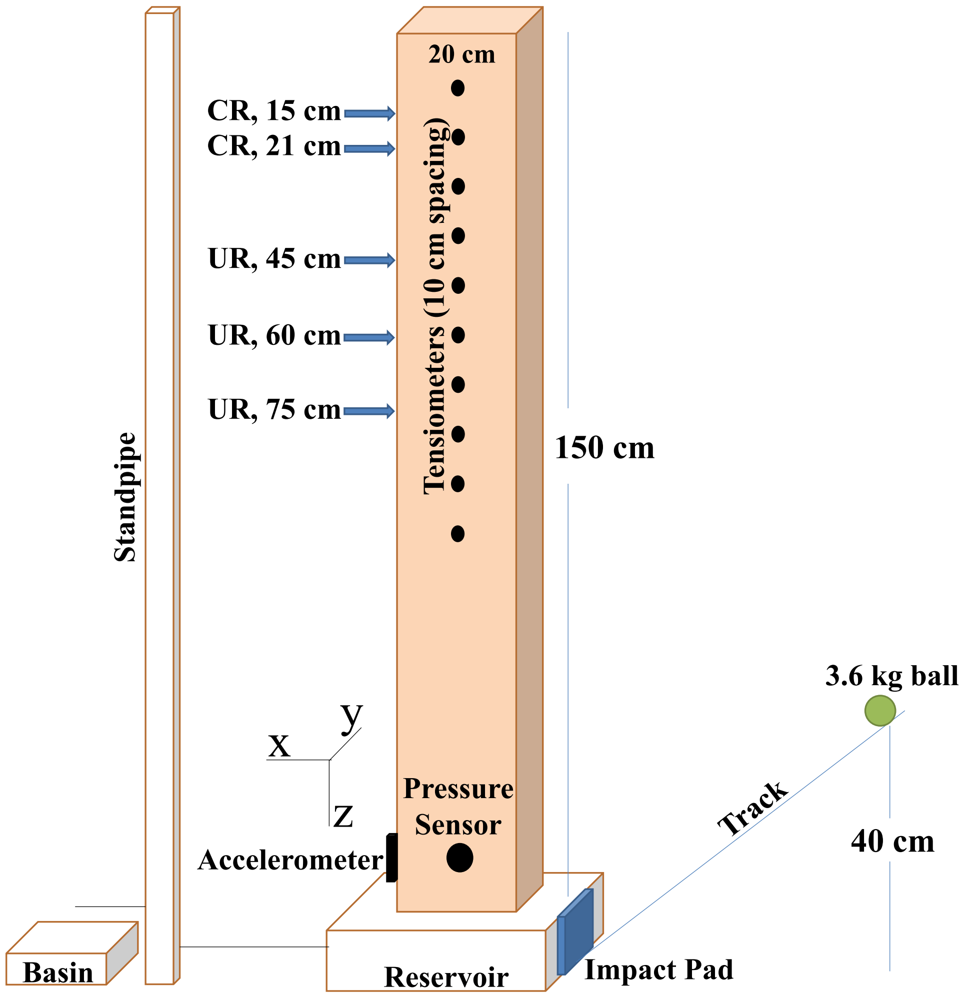

Figure 3.2: Our experimental apparatus is a 1.5 m tall sand chamber, instrumented with a pressure sensor, an accelerometer, and tensiometers. A 3.6 kg iron ball is released from 40 cm above the base to shake the chamber. Blue arrows mark the depth of the water table below the surface for our experiments in the Capillary (CR) and Unsaturated (UR) regimes.

3.4 Results

We began our experiment with the water table several centimeters above the sand surface, which we refer to as the *Standing regime*. In order to reach a steady state of compaction, we repeatedly impacted the sand column at the beginning of the experiment, observing sudden increases in pore pressure after each impact. As the sand became more compacted, the amplitude of the pressure response decreased with successive impacts until stabilizing at 0.5 cmH_2O. After the amplitude of the pressure response stabilized in the Standing regime, we lowered the water table below the sand surface to progressively greater depths, as indicated

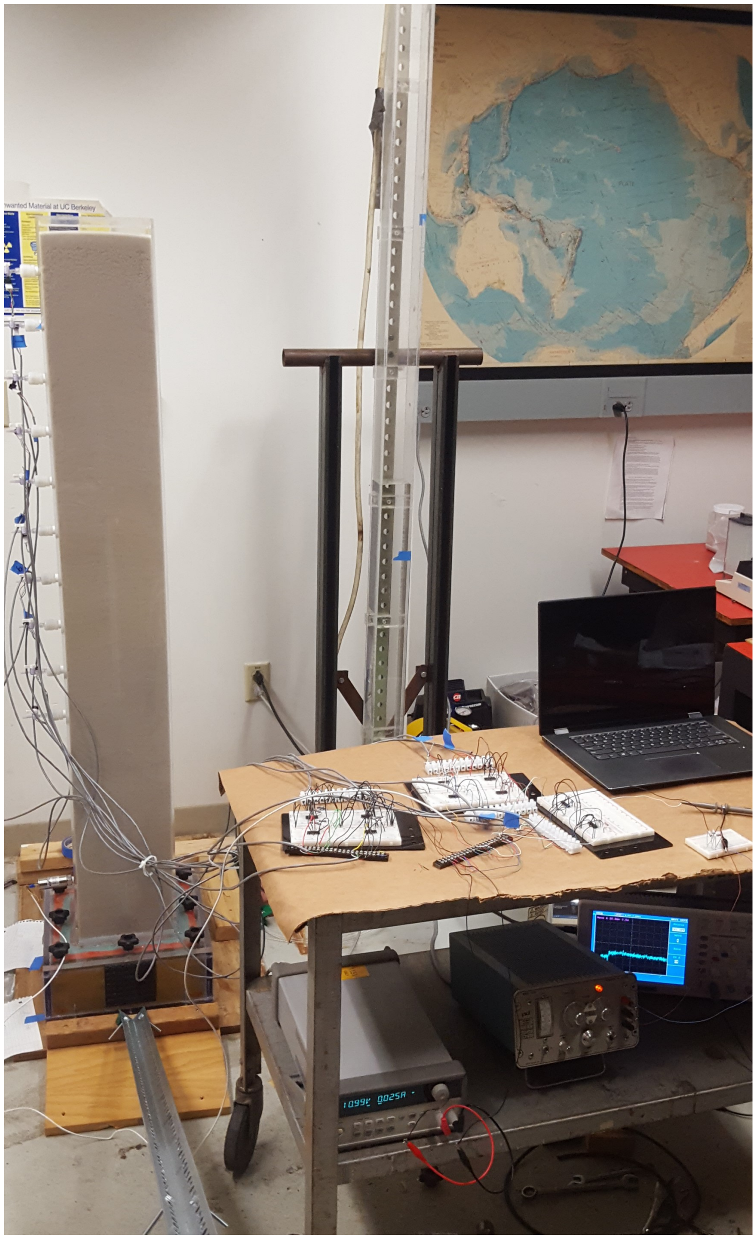

Figure 3.3: This photograph of the experimental apparatus shows the sand column on the left. The ten tensiometers and the pressure sensor are visible on the column's left side. The tall standpipe is to the right of the column. In the foreground is the steel track, two DC power supplies, a digital storage oscilloscope, and operational amplifier circuits.

by red lines in Figure 3.4. In the *Capillary regime*, the water table is shallow, and a saturated capillary fringe exists between it and the surface. In the *Unsaturated regime*, the water table is deep enough to cause drainage, creating an unsaturated zone between the surface and

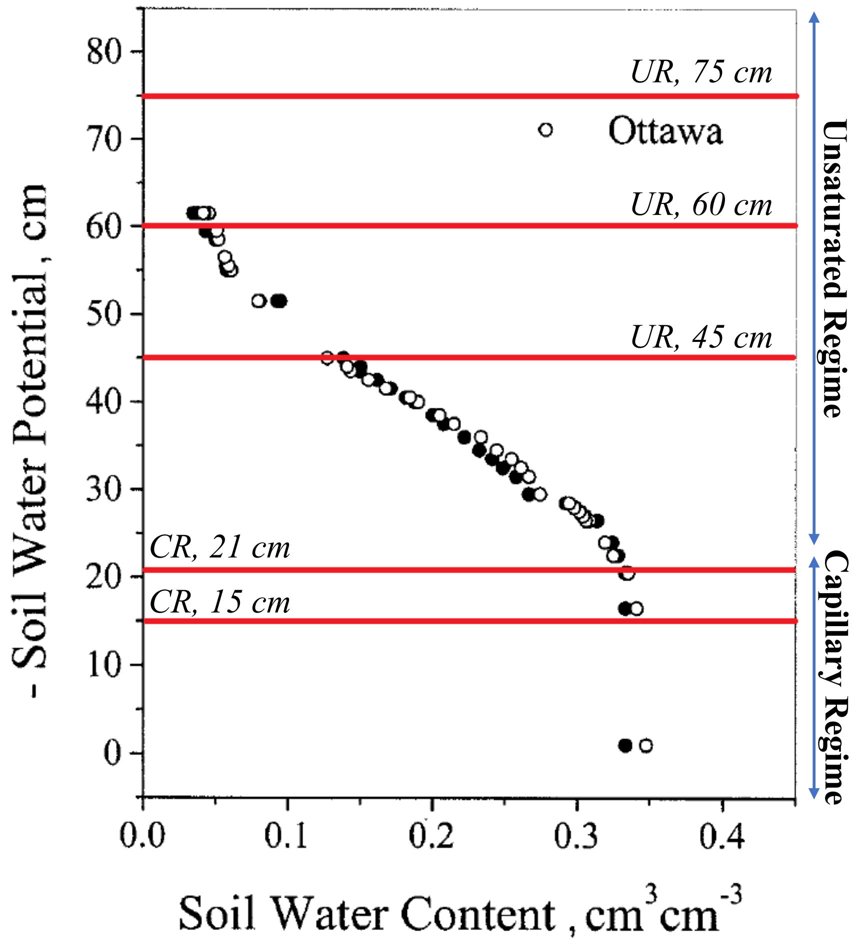

Figure 3.4: Modified from Vaz et al. (2002), this figure shows the water retention function for our sand measured by drainage outflow (open circles) and a time domain reflectometer (filled circles). Moving upward from the water table at 0 cm potential, there is a ∼20 cm saturated capillary fringe, a transitional unsaturated zone (from ∼20 to ∼60 cm), and a residual zone (>60 cm). When the water table is ∼45 cm below the surface, for instance, the water content profile from the water table up to the sand surface will be the plotted curve from the 0 cm line up to the 45 cm line.

the capillary fringe. Impacts in the Capillary and Unsaturated regimes were performed on consecutive days to allow for equilibration following impacts and to reach steady water table levels. All experiments were conducted without repacking the sand because the sand was stabilized in the Standing regime.

Figure 3.5 shows two Standing regime pressure signals from the pressure sensor, relative to hydrostatic, near the first and last impacts. Impact 3 generated a sudden pressure rise to ∼3 cmH_2O, which declines rapidly afterwards, while Impact 60 generated a much smaller ∼0.5 cmH_2O pressure signal that declines more slowly. The accelerometer data in Figure 3.5 shows that accelerations are largest in the horizontal plane, in the direction of the impact (x), and peak at ∼20 m/s^2. Small shocks following the mainshock at ∼0.4 s are caused by the iron ball rebounding on the impact pad. Note that the pressure rise time exceeds the duration of shaking. This is consistent with field observations of the Superstition Hills earthquake, where pore pressure continued to increase after ground shaking subsided (Holzer and Youd, 2007).

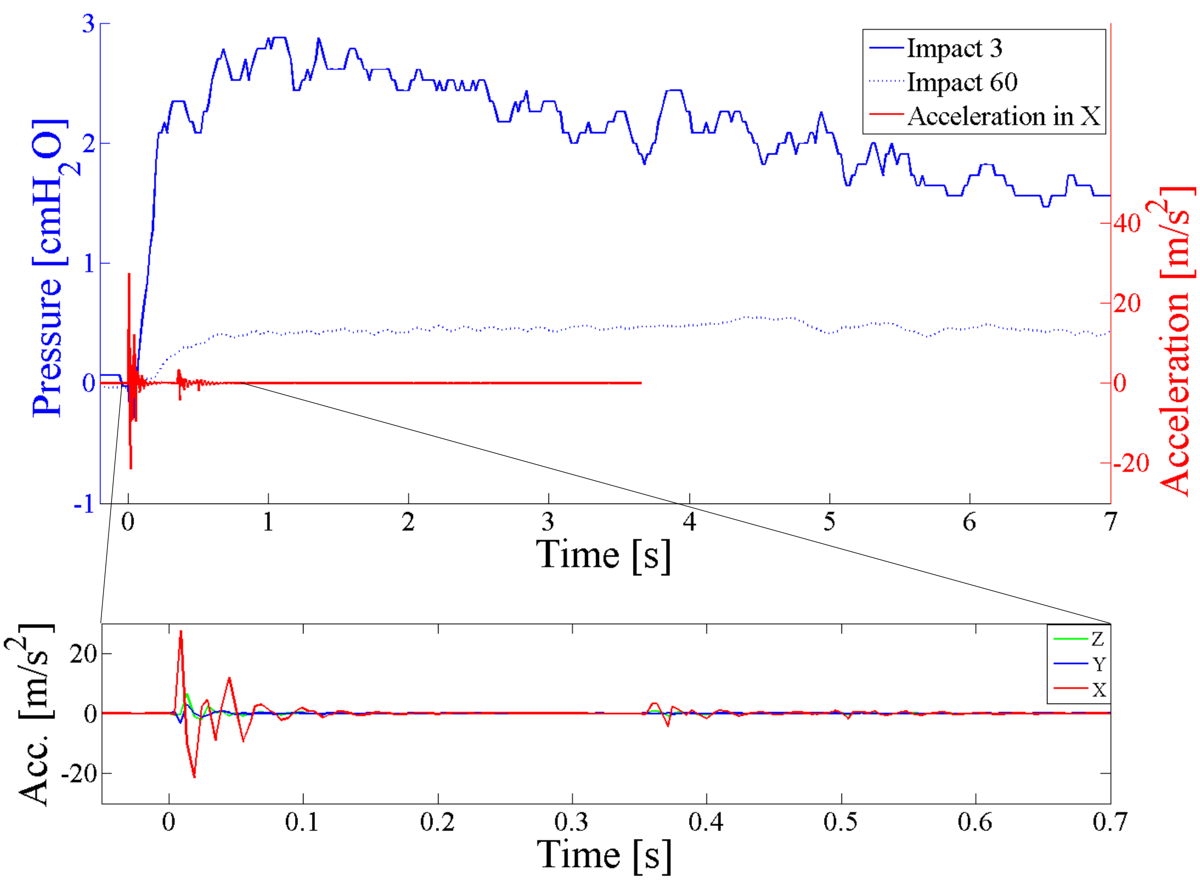

Figure 3.5: This plot shows pore pressure relative to hydrostatic during the third (solid blue line) and last (dashed blue line) impacts from the Standing regime. Time is relative to impact. The amplitude of the pressure response and the decay rate both decrease in later impacts, but the rise time of the pressure signals remained at ∼1 s. The last impact of the Standing regime is plotted over a longer time window with acceleration data. Note that the duration of the pressure increase greatly exceeds the duration of shaking.

Following Impact 60, we lowered the water level to 15 cm below the sand surface and found a different pressure response. Here, in the Capillary regime, pressure rises sharply after impact (Figure 3.6a), and the amplitude increases to centimeters. The rise time is $\sim$1 s in the Standing regime (Figure 3.5) and less than 0.1 s in Capillary and Unsaturated regimes (Figure 3.6). After the initial rise, pressure first declines and then slowly increases before it finally declines to its starting value over the course of several hours (the final decline was monitored by hand and is not shown).

In the Unsaturated regime, the water table was farther below the sand surface, at 45, 60, and 75 cm. Following impact, pressure rose sharply (Figure 3.6b), but it did not increase following the decline from the peak, as in the Capillary regime. Instead, it decayed exponentially with time, consistent with the hydraulic diffusivity of the sand. Also, pressure did not recover to its starting value. At each height there was a sustained increase of $\sim$0.5 cmH_2O, shown at 900 s, which indicates the amount of water liberated by each impact.

The tensiometer data in Figure 3.7, from an impact at 75 cm, supports the theory of Richards (1931) that the pressure gradient in the unsaturated zone beneath the residual region is hydrostatic. However, the highest tensiometer is clearly off the hydrostatic line, in the residual zone, before and after the impact. In response to the impact, all tensiometers in the hydrostatic unsaturated zone register a small and consistent decrease in tension due to increasing saturation. The highest tensiometer, in contrast, registers an increase in tension due to decreasing saturation. This is unlikely to have been caused by evaporation because the expected evaporation rate, considering laboratory conditions, water table depth, and grain size, is only $\sim$1 mm/day (Hellwig, 1973). Rather, the decrease in tension in the hydrostatic zone and increase in tension in the residual zone are evidence that shaking causes pockets of water in the residual zone to drain to the hydrostatic zone below, ultimately raising the water table by centimeters. We acknowledge that pore pressure may continue to evolve for days after the impact, but the post-impact rightward shift toward lower tension is observed in all seven tensiometers and is much larger than the deviations from the hydrostatic lines.

3.5 Discussion

We interpret the pressure rise in the Standing regime to be caused by sand compaction during impact-induced shaking. When the impact occurs, compaction generates excess pore pressure that subsequently decays according to the hydraulic diffusivity. With subsequent impacts, as the sand becomes more compacted, porosity decreases, and excess pore pressure also decreases. Repeated impacts also led to longer decay times (diffusivity evolves from 7.0×10^{-2} to 3.5×10^{-2} m^2/s), which implies decreasing permeability. After 40 impacts, compaction ceased, but sand mobilization still caused a small and repeatable pressure increase of $\sim$0.5 cmH_2O. This is similar to processes occurring in slurries and submarine avalanches (e.g., Major, 2000). After 60 impacts, progressive grain size segregation was clearly visible in a 10 cm thick layer at the top of the chamber. The upper half was finer sand, and the lower half was coarser sand with small voids. Grain size analysis conducted after the experiment

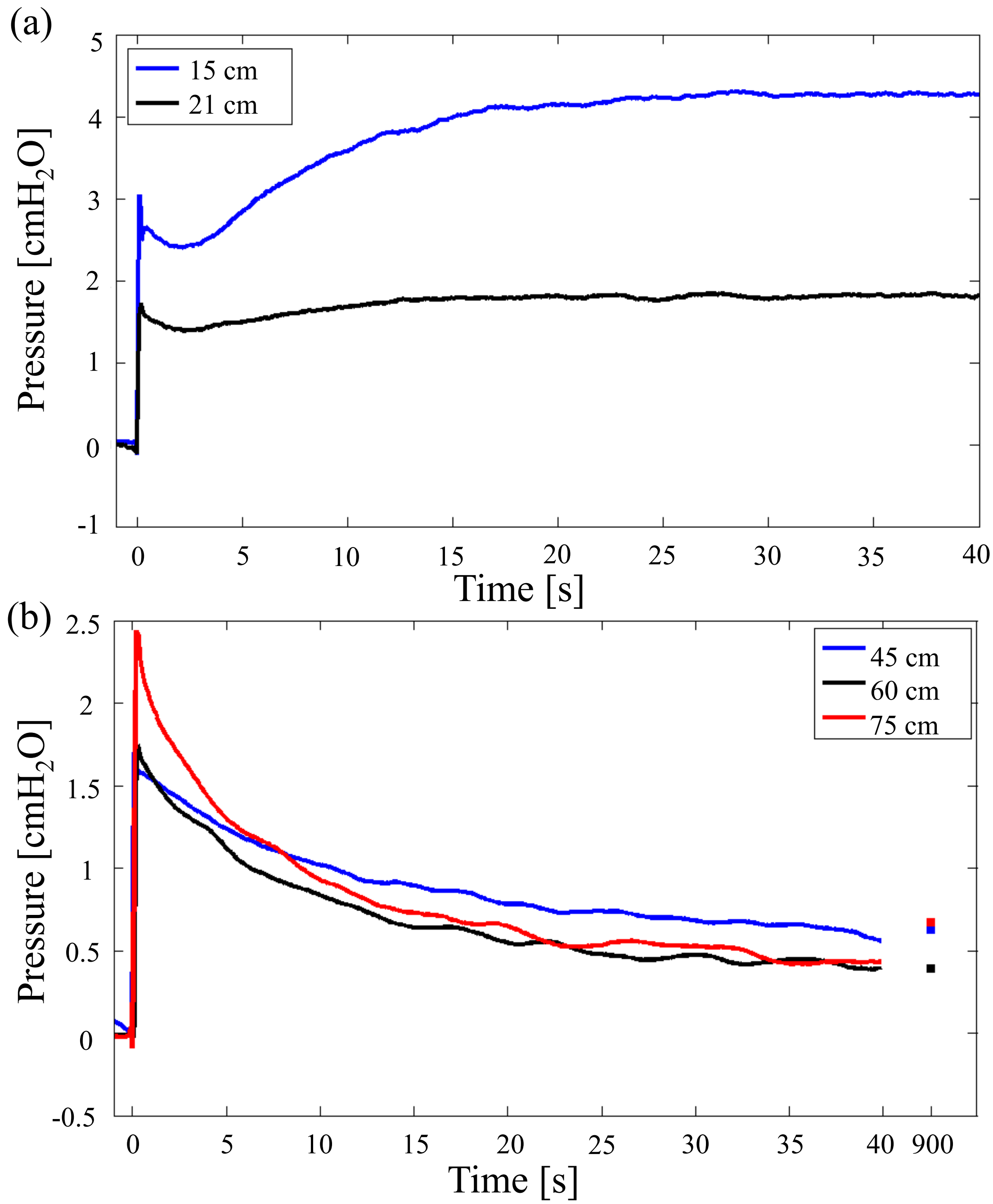

Figure 3.6: (a) Experimental results from the Capillary regime. Pore pressure increases rapidly after impact, by centimeters. (b) Experimental results from the Unsaturated regime. Pore pressure increases rapidly and then decays according to the hydraulic diffusivity timescale, and it remains elevated indefinitely.

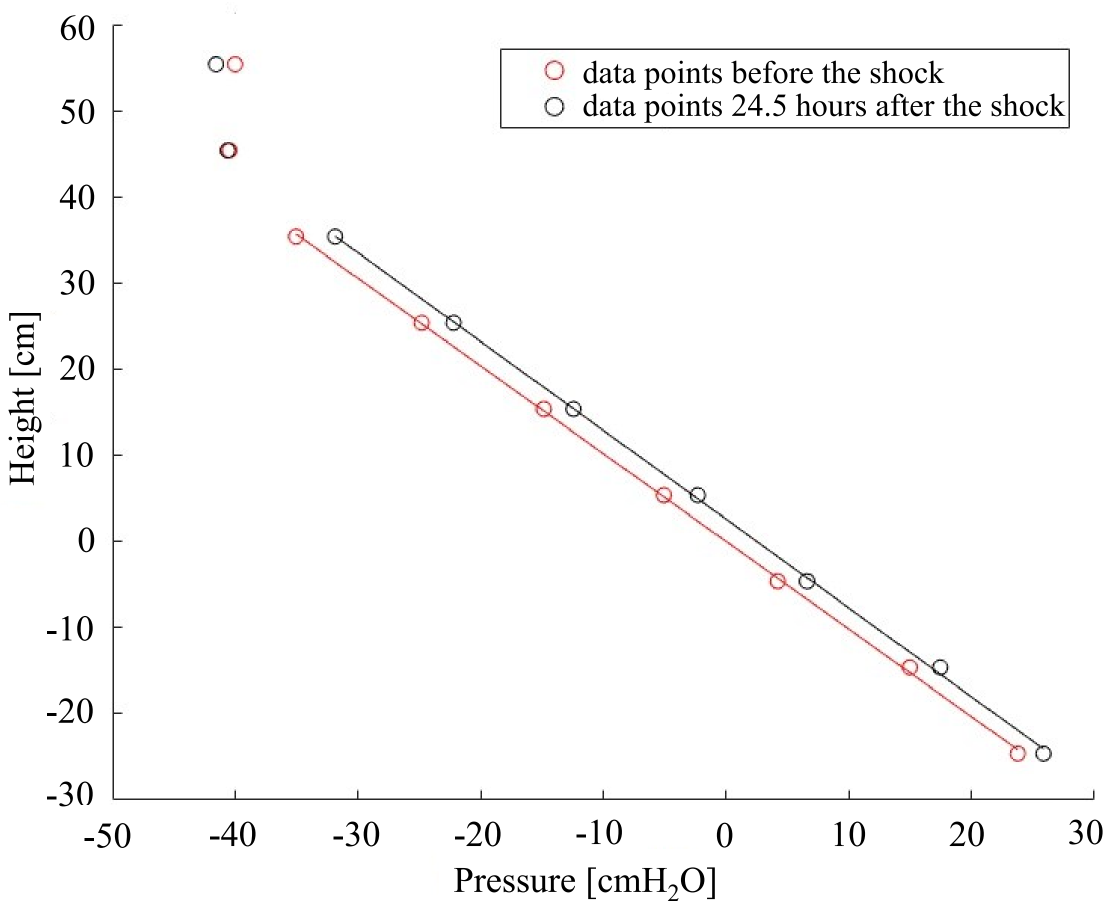

Figure 3.7: Tensiometers allow us to monitor pore pressure relative to height above the water table (y-axis). The drying observed at ∼55 cm height is evidence of water transport out of the residual zone.

showed that the fines content, which is the percentage of grains passing through sieve size 70 (212 micron), increased from 7% near the base of the layer to 11% near the top. This segregation may cause slight deviations from the water retention function of Figure 3.4 near the surface.

In the Capillary regime, we attribute the first, rapid pressure rise to the disruption of air/water menisci at the sand surface during shaking, which releases water held in tension in the capillary fringe and causes the water table to rise quickly, without flow. In the Unsaturated regime, pore pressure increases rapidly and then decays according to the hydraulic diffusivity timescale, and it remains elevated indefinitely. This phenomenon has been observed in the beach swash zone, where wave runup rapidly increases pore pressure in the saturated sand (Turner and Nielsen, 1997). We infer that the capillary force is only partially destroyed by the impact because complete destruction of the surface menisci would result in a pressure increase equal to the full height of the capillary fringe, which extends up to ~20 cm (Figure 3.4).

The upward shift of the water table in the Unsaturated regime may be evidence of water being shaken out of the unsaturated sediments. This supports the hypothesis of Mohr et al. (2015) that increased streamflow in the Chilean coastal range following the 2010 $M_w 8.8$ Maule earthquake was caused by water shaken out of unsaturated soil. Based on total excess discharge, Mohr estimated that a spatial average of 8-9 mm of water was released throughout the catchment. They suggested that seismic energy reduces capillary pressure, and therefore an energy density of 100 J/m^3 should increase the water retention threshold by 100 Pa, or 1 cmH_2O. The fast pressure rise in the Unsaturated regime may be due to the disruption of air/water menisci, which releases water held in tension in the capillary fringe, causing the water table to rise without flow, as in the Capillary regime.

The post-impact responses of pressure in the Capillary and the Unsaturated regimes are markedly different. In the Capillary regime, the menisci occur at or near the sand surface, and therefore the layer above the water table was nearly saturated before the impact. After the impact, the menisci are destroyed. The slow, secondary increase in pressure suggests that the capillary fringe was not complete saturated before the impact, and that isolated pockets of pore water continued to drain after the impact under the new surface boundary condition. The final, slow pressure decline indicates the occurrence of imbibition (defined as an increase in water saturation) and the rebuilding of menisci over a timescale that is slower than porous flow and likely controlled by evaporation at the surface.

In the Unsaturated regime, there are two key differences. First, the menisci are distributed throughout the unsaturated zone, and hence the total area of the air-water interface is much greater than in the Capillary regime. Thus, for a finite amount of vibrational energy, enough to destroy all of the menisci in the Capillary regime, only a small fraction of the menisci in the Unsaturated regime will be destroyed. Second, the destruction of menisci after an impact causes pore water in the unsaturated zone to drain to the water table (the drainage process), raising the pressure in the saturated zone. Surface tension, on the other hand, causes pore water to rise above the water table (the imbibition process), decreasing the pressure in the saturated zone. The two processes follow separate paths and may cause significantly different capillary pressures at the same saturation - hysteresis (e.g., Bear, 1972). Our observation that pressure did not recover to its starting value in the Unsaturated regime may be influenced by hysteresis in the unsaturated zone.

3.6 Conclusion

In conclusion, our laboratory experiments show that pore pressure in both saturated and unsaturated sediments may suddenly increase during impulsive shaking, such as during earthquakes. We show that in saturated sediments this may be due to shaking-induced consolidation, while in unsaturated sediments this may be due to the destruction of menisci in sediment pores. We also provide a quantitative criterion to differentiate these two mechanisms, even though both mechanisms require a recording rate much higher than that of current field systems. Thus, to explain regional hydrological changes after earthquakes, our results support both the consolidation hypothesis and the new hypothesis of water released from unsaturated soil. The difference in the seismic energy required to cause undrained consolidation (Green and Mitchell, 2004) and to release water from the unsaturated zone may provide a means to differentiate the two mechanisms, but more data and experiments are required to further this work. Considering the importance of the capillary force above the water table, these new mechanisms may be useful for explaining other hydrological responses to earthquakes, beyond streamflow and water-level increases.

Chapter 4

Outlook

To close this dissertation, I will highlight some of the science opportunities presented by the previous two chapters, as well as some methodological conclusions. In Chapter 2, we presented a new model for the saturation state of a voxel after it is first traversed by the invading nonwetting phase (S_{nc}) during gravitationally stable drainage, and we demonstrated that in order to match the observed propagation speed of our drainage front, the standard model simulations required a much larger S_{nc} value than we observed with our flow cell. This result should help motivate the continued development of numerical models of two phase flow in porous media. The observed discrepancy arises in part because the physics occurring at the propagating interface is not incorporated into the standard model, and therefore it cannot be expected to correctly define the time to decrease S_w from 1 to $1 - S_{nc}$. Also, because the simulation uses upstream relative permeability weighting in accordance with the hyperbolic nature of the governing equations, the nonwetting relative permeability (κ_n) of the frontal voxel may be enlarged because the air saturation (S_n) one voxel upstream is higher. This error will grow in proportion to the saturation difference between these two voxels, which, as shown in Chapter 2, is influenced by Bo, Ca, and L_z. Thus, in practice, artificially large values of S_{nc} may be needed to counter the erroneously high relative permeability (κ_n) by requiring the frontal voxel to over-accumulate the nonwetting phase before the flow is allowed to advance downstream. As emphasized by Dinh et al. (2003), which describes the challenges of modeling interpenetrating continua, we are now in murky territory where, "*The dangerous interplay between errors of numerical and physical origins hampers the fidelity of the two-fluid calculation results.*"

Going forward, it will be important to develop numerical methods for multiscale simulations of two-phase flow (e.g., Carrillo et al., 2020) that incorporate some degree of interface resolution, while also searching for equations to describe pore-scale flow in regions where saturation is evolving. We should make progress on both fronts, in other words, aiming to reduce numerical errors and increase physical understanding. To constrain our new models, we should continue gathering new data from the field and performing targeted laboratory experiments (Kirchner, 2006). A straightforward extension of Chapter 2, for instance, is to explore a larger range of Bo and Ca, or to examine the same Bo and Ca with a more complex porous material, such as sand or soil, to test the universality of our scaling exponents and constants.

While the capillary pressure function ($P_c(S_w)$) was not the primary focus of Chapter 2, Figure 2.3 is nonetheless a direct test of the important van Genuchten model in a uniform porous medium, with resolution of the entire curve (van Genuchten, 1980, >25,000 citations). We found that the model underpredicts saturation in the region between w and h, where the observed saturation becomes almost linear with respect to P_c. The IP $s(z)$ curves in Figure 2.14 also show a nearly-linear approach to residual saturation at h. These observations suggest that van Genuchten -based models of the unsaturated zone may be prone to underestimating equilibrium water content in the capillary fringe (i.e., the *field capacity*, θ_{fc}), which would have important consequences for models of evapotranspiration, for example (Maina and Siirila-Woodburn, 2020). Broadly speaking, the pore-scale resolution of fluid structure in IP should allow us to incorporate more detail into models of the physical and biological processes occurring in the unsaturated zone. This becomes more feasible as large-scale IP simulations become faster (e.g., Masson, 2016).

The next phase of IP research may be inspired by some of the observations in Section 2.4, where we compared laboratory and IP -derived $s(z)$ curves. One interesting result is the 4:1 correspondence between IP lattice spacing and grain diameter (Figure 2.14). This spacing is consistent with the observation that a meniscus will cross many pores in a single Haines jump (Armstrong et al., 2015), which may imply a reconceptualization of lattice sites as locations where jumps can begin and end. Alternatively, it could motivate a more sophisticated displacement mechanism in IP where many adjacent sites are occupied in a single jump. Modifying the rules of motion in IP to more accurately reflect our understanding of Haines jumps in this manner is a good place to begin. It will be interesting to learn whether the resulting invasion structures lose their resemblance to classical percolation structures.

In Chapter 3, we measured the response of pore pressure in saturated and unsaturated sand to seismic shaking to better understand coseismic changes in groundwater level and streamflow, particularly in areas with no elevated topography. We conducted experiments with the water table above and below the sand surface. When the water table was above the surface, pore pressure increased due to undrained consolidation by 0.5 to 3 $\mathrm{cmH_2O}$, depending on the state of compaction before impact. One surprising observation was that the pressure rise time ($\sim$1 s) exceeded the duration of shaking. This slow rise has also been observed in the field (e.g., Holzer and Youd, 2007), and its cause should be further investigated.

When the water table was below the surface, pore pressure again increased by centimeters, but with a faster rise time (< 0.1 s), due to disruption of capillary forces. To help determine whether this is a widespread phenomenon, we should try to delineate the threshold seismic energy density for water release from the unsaturated zone. Also, as shown in Figure 3.7, tensiometers were a remarkably effective tool for monitoring capillary pressure in the unsaturated zone. They provided evidence of drying in the residual zone, and they confirmed an important assumption of Chapter 2, that water held in tension between the water table and the residual zone is continuous, with a hydrostatic pressure gradient. Tensiometers could be utilized by hydrogeologists in much the same way as monitoring wells and stream gauges. Installing them in a range of field settings on a long term, networked basis would help improve our understanding of transport and structure in the unsaturated zone.

Finally, I would like to reiterate that Chapter 3 was a laboratory-based collaboration with an international student who visited Berkeley from Peking University in 2019. Because this could not have happened in 2020, I will end by emphasizing that the outlook for science is brightest when such collaborations are possible.

References

Abu-Al-Saud, M. O., Riaz, A., and Tchelepi, H. A. (2017). Multiscale level-set method for accurate modeling of immiscible two-phase flow with deposited thin films on solid surfaces. *Journal of Computational Physics* 333, pp. 297–320.

Armstrong, R. T., Evseev, N., Koroteev, D., and Berg, S. (2015). Modeling the velocity field during Haines jumps. *Advances in Water Resources* 77, pp. 57–68.

Bastidas, A. M. P. (2016). Ottawa F-65 Sand Characterization. PhD thesis. University of California, Davis.

Bear, J. (1972). *Dynamics of Fluids in Porous Media.* American Elsevier Publishing Company.

Birovljev, A., Furuberg, L., Feder, J., Jssang, T., Måløy, K. J., and Aharony, A. (1991). Gravity invasion percolation in two dimensions: Experiment and simulation. *Phys. Rev. Lett.* 67 (5), pp. 584–587.

Blanchard, F. G. and Byerly, P. (1935). A study of a well gauge as a seismograph. *Bull. Seismo. Soc. Am.* 25, pp. 313–321.

Carrillo, F. J., Bourg, I. C., and Soulaine, C. (2020). Multiphase flow modeling in multiscale porous media: An open-source micro-continuum approach. *Journal of Computational Physics: X* 8, p. 100073.

Claesson, L., Skelton, A., Graham, C., Dietl, C., Mörth, M., Torssander, P., and Kockum, I. (2004). Hydrogeochemical changes before and after a major earthquake. *Geology* 32.8, pp. 641–644.

Claesson, L., Skelton, A., Graham, C., and Morth, C.-M. (2007). The timescale and mechanisms of fault sealing and water-rock interaction after an earthquake. *Geofluids* 7.4, pp. 427–440.

Corey, A. T. (1954). The interrelation between gas and oil relative permeabilities. *Producers Monthly.*

Cottin, C., Bodiguel, H., and Colin, A. (2010). Drainage in two-dimensional porous media: From capillary fingering to viscous flow. *Phys. Rev. E* 82 (4), p. 046315.

DeGennes, P. G. (1983). Theory of Slow Biphasic Flows in Porous Media. *Physicochemical Hydrodynamics* 4, pp. 175–185.

Dinh, T. N., Nourgaliev, R. R., and Theofanous, T. G. (2003). Understanding the Ill-Posed Two-Fluid Model. *The 10th International Topical Meeting on Nuclear Reactor Thermal Hydraulics (NURETH-10)*.

Dury, O., Fischer, U., and Schulin, R. (1999). A comparison of relative nonwetting-phase permeability models. *Water Resources Research* 35.5, pp. 1481–1493.

Frette, O. I., Måløy, K. J., Schmittbuhl, J., and Hansen, A. (1997). Immiscible displacement of viscosity-matched fluids in two-dimensional porous media. *Phys. Rev. E* 55 (3), pp. 2969–2975.

Ghanbarian, B., Sahimi, M., and Daigle, H. (2016). Modeling relative permeability of water in soil: Application of effective-medium approximation and percolation theory. *Water Resources Research* 52.7, pp. 5025–5040.

Glass, R. J., Conrad, S. H., and Peplinski, W. (2000). Gavity-destabilized nonwetting phase invasion in macroheterogeneous porous media: Experimental observations of invasion dynamics and scale analysis. *Water Resources Research* 36.11, pp. 3121–3137.

Green, R. A. and Mitchell, J. K. (2004). Energy-Based Evaluation and Remediation of Liquefiable Soils. *Geotechnical Engineering for Transportation Projects*, pp. 1961–1970.

Hellwig, D. H. R. (1973). Evaporation of Water from Sand, 4: The Influence of the Depth of the Water-Table and the Particle Size Distribution of the Sand. *Journal of Hydrology* 18, pp. 317–327.

Holzer, T. L. and Youd, T. L. (2007). Liquefaction, Ground Oscillation, and Soil Deformation at the Wildlife Array, California. *Bulletin of the Seismological Society of America* 97.3, pp. 961–976.

Hoogland, F., Lehmann, P., and Or, D. (2015). The formation of viscous limited saturation zones behind rapid drainage fronts in porous media. *Water Resources Research* 51.12, pp. 9862–9890.

Kirchner, J. W. (2006). Getting the right answers for the right reasons: Linking measurements, analyses, and models to advance the science of hydrology. *Water Resources Research* 42.3.

Kirkpatrick, S. (1973). Percolation and conduction. *Rev. Modern Phys.* 45, pp. 574–586.

Kramer, C. A. (2013). An Experimental Investigation of Performance of a Model Geothermal Pile in Sand. MA thesis. The Pennsylvania State University.

Lenormand, R., Touboul, E., and Zarcone, C. (1988). Numerical models and experiments on immiscible displacements in porous media. *Journal of Fluid Mechanics* 189.

Løvoll, G., Meheust, Y., Maloy, K., Aker, E., and Schmittbuhl, J. (2005). Competition of gravity, capillary and viscous forces during drainage in a two-dimensional porous medium, a pore scale study. *Energy* 30, pp. 861–872.

Maina, F. Z. and Siirila-Woodburn, E. R. (2020). The Role of Subsurface Flow on Evapotranspiration: A Global Sensitivity Analysis. *Water Resources Research* 56.7.

Major, J. J. (2000). Gravity-Driven Consolidation of Granular Slurries - Implications for Debris-Flow Deposition and Deposit Characteristics. *Journal of Sedimentary Research* 70.1, pp. 64–83.

Manga, M., Wang, C., and Shirzaei, M. (2016). Increased stream discharge after the 3 September 2016 Mw 5.8 Pawnee, Oklahoma earthquake. *Geophysical Research Letters* 43.22, pp. 11, 588–11, 594.

Masson, Y. (2016). A fast two-step algorithm for invasion percolation with trapping. *Computers and Geosciences* 90, pp. 41–48.

Méheust, Y., Løvoll, G., Måløy, K. J., and Schmittbuhl, J. (2002). Interface scaling in a two-dimensional porous medium under combined viscous, gravity, and capillary effects. *Phys. Rev. E* 66 (5), p. 051603.

Mohr, C. H., Manga, M., Wang, C., Kirchner, J. W., and Bronstert, A. (2015). Shaking water out of soil. *Geology* 43.3, pp. 207–210.

Muir-Wood, R. and King, G. C. P. (1993). Hydrological signatures of earthquake strain. *J. Geophys. Res.* 98, pp. 22035–22068.

Nimmo, J. R. (2010). Theory for Source-Responsive and Free-Surface Film Modeling of Unsaturated Flow. *Vadose Zone Journal* 9, pp. 295–306.

Pruess, K. (2004). The TOUGH codes - a family of simulation tools for multiphase flow and transport processes in permeable media. *Vadose Zone Journal* 3.3, pp. 738–746.

Reynolds, C. A., Menke, H., Andrew, M., Blunt, M. J., and Krevor, S. (2017). Dynamic fluid connectivity during steady-state multiphase flow in a sandstone. *Proceedings of the National Academy of Sciences* 114.31, pp. 8187–8192.

Richards, L. A. (1931). Capillary conduction of liquids through porous mediums. *Journal of Applied Physics* 1, pp. 318–333.

Rojstaczer, S. and Wolf, S. (1992). Permeability changes associated with large earthquakes: An example from Loma Prieta, California. *Geology* 20.3, pp. 211–214.

Rosso, M., Gouyet, J. F., and Sapoval, B. (1985). Determination of percolatiuon probability from the use of a concentration gradient. *Phys. Rev. B* 32, pp. 6053–6054.

Schmidt, F. J. (1875). Studien uber Erdbeben. *Leipzig: Carl Scholtze*, p. 360.

Tidwell, V. C. and Glass, R. J. (1994). X ray and visible light transmission for laboratory measurement of two-dimensional saturation fields in thin-slab systems. *Water Resources Research* 30.11, pp. 2873–2882.

Tokunaga, T. (1999). Modeling of earthquake-induced hydrological changes and possible permeability enhancement due to the 17 January 1995 Kobe Earthquake, Japan. *Journal of Hydrology* 223, pp. 221–229.

Toussaint, R., Måløy, K., Méheust, Y., Løvoll, G., Jankov, M., Schäfer, G., and Schmittbuhl, J. (2012). Two-Phase Flow: Structure, Upscaling, and Consequences for Macroscopic Transport Properties. *Vadose Zone Journal* 11.3.

Turner, I. L. and Nielsen, P. (1997). Rapid water table fluctuations within the beach face: Implications for swash zone sediment mobility? *Coastal Engineering* 32.1, pp. 45–59. ISSN: 0378-3839.

van Genuchten, M. T. (1980). A Closed-form Equation for Predicting the Hydraulic Conductivity of Unsaturated Soils. *Soil Sci. Soc. Am. J.* 44, pp. 892–898.

Vaz, C. M. P., Hopmans, J. W., Macedo, A., Bassoi, L. H., and Wildenschild, D. (2002). Soil Water Retention Measurements Using a Combined Tensiometer-Coiled Time Domain Reflectometry Probe. *Soil Sci. Soc. Am. J.* 66, pp. 1752–1759.

Wang, C., Cheng, L.-H., Chin, C.-V., and Yu, S.-B. (2001). Coseismic hydrologic response of an alluvial fan to the 1999 Chi-Chi earthquake, Taiwan. *Geology* 29.9, pp. 831–834.

Wang, C. and Manga, M. (2010). *Earthquakes and Water*. Springer-Verlag Berlin Heidelberg.

— (2015). New streams and springs after the 2014 Mw6.0 South Napa earthquake. *Nat. Commun.* 6.7597.

Wang, C., Manga, M., Shirzaei, M., Weingarten, M., and Wang, L. (2017). Induced Seismicity in Oklahoma Affects Shallow Groundwater. *Seismological Research Letters* 88.4, pp. 956–962.

Wang, C., Wang, C.-H., and Manga, M. (2004). Coseismic release of water from mountains: Evidence from the 1999 (Mw = 7.5) Chi-Chi, Taiwan, earthquake. *Geology* 32.9, pp. 769–772.

Wilkinson, D. (1984). Percolation model of immiscible displacement in the presence of buoyancy forces. *Phys. Rev. A* 30, pp. 520–531.

Wilkinson, D. and Willemsen, J. F. (1983). Invasion percolation: a new form of percolation theory. *J. Phys. A: Math. Gen.* 16, pp. 3365–3376.

Yortsos, Y. C., Xu, B., and Salin, D. (2001). Delineation of Microscale Regimes of Fully-Developed Drainage and Implications for Continuum Models. *Computational Geosciences* 5.3, pp. 257–278.